Rock Mechanics and Rock Engineering (2022) 55:1087–1110
https://doi.org/10.1007/s00603-021-02736-0

ORIGINAL PAPER

# Temperature-Induced Ductile–Brittle Transition in Porous Carbonates and Change in Compaction Band Growth Revealed by 4-D X-Ray Tomography

Xiao Chen[1] · Klaus Regenauer-Lieb[1,2] · Hamid Roshan[1]

Received: 14 April 2021 / Accepted: 4 December 2021 / Published online: 4 January 2022


## Abstract

Deformation bands featuring localised material failure are ubiquitous in nature. They form important flow barriers and reduce/compartmentalise fluid flow in oil/gas/water reservoir rocks. Moderate temperature changes have been observed to play a fundamental role in the formation and style of these bands, but the mechanisms underpinning these changes are often obscure. Here, we show compaction experiments of highly porous limestone from Mt Gambier, Australia, with chemically non-reacting gaseous (helium) and fluid (kerosene) pore fluids. Gas-filled limestones showed a lower static elastic stiffness than fluid-filled specimens. The discrepancy in elastic modulus is particularly noted at high temperature. This indicates the important effect of temperature-sensitive compressibility of gas-filled pores versus nominally incompressible fluid-filled pores. A moderate temperature rise from 25 to 80 °C also led to a sharp transition in compaction band growth from dominantly ductile diffuse band growth at low temperatures to prevailing brittle growth at higher temperatures. We attribute this change to a temperature-sensitive change in micro-mechanism from rate-sensitive calcite twinning at room temperature to activation of a near-ideal plastic Peierls mechanism at 80 °C. The inverse-to-normal brittle–ductile transition is documented by time-lapse X-ray CT micro-tomographic images and associated digital image and volume image correlation techniques.

## Highlights

- 4D time-lapse triaxial experiments on highly porous carbonates reveal thermomechanical and thermohydromechanical couplings.
- Gas saturated specimens show higher yield stress and lower elastic modulus when compared to fluid-saturated specimens.
- A changeover from ostensibly ductile to a dominantly brittle micro-deformation mechanisms is encountered when raising the temperature from 25 to 80 °C.

**Keywords** Poromechanics · Fluid compressibility effect · Wave propagation · Digital image analysis · Digital volume correlation · Permeability

## 1 Introduction

Carbonates are one of the major sedimentary formations widely distributed in the near-surface and upper layers of the Earth's crust. These porous rocks form one of the most considerable hydrocarbon resources accounting for almost 60% of the conventional world's hydrocarbon reserves (Sayers 2008). These hydrocarbon reservoirs are also amongst the best candidate storage facilities for geological sequestration of carbon dioxide when depleted (Lackner 2002; Paluszny et al. 2020; Wawersik et al. 2001). However, the subsurface

✉ Klaus Regenauer-Lieb
klaus@curtin.edu.au

[1] School of Mineral and Energy Resources Engineering, UNSW Sydney, Kensington, Sydney, NSW, Australia

[2] Western Australian School of Mines: Minerals, Energy and Chemical Engineering, Curtin University, Perth, WA, Australia

engineering applications of carbonates largely depend on their coupled mechanical, thermal, and chemical behaviours, which can strongly influence the fluid flow properties (Hadgu et al. 1995; Kümpel 2012; Zimmerman 2000). We target in our investigation the low-temperature regime of up to 80 °C using novel experimentation. Of particular interest are the microstructural response, the possible change of the internal fluid pathways, and the overall permeability effect in both micro- and macro-scale. The analysis will identify the possibility of forming internal microstructural changes such as compaction bands, shear bands, pore collapse, and fractures as a function of temperature and fluid type (gas versus liquid).

### 1.1 Low-Temperature Effect on Carbonates

A critical mechanical-related feature of the porous carbonate rocks is the stress/pressure-sensitivity of their skeleton. This enables an early transition from dilation to compaction failure, because the calcite can easily form mechanical twins or causes dislocation glide at relatively low-stress and temperature conditions (Burkhard 1993; Ferrill et al. 2004; Turner et al. 1954). These localised deformations can occur over a vast range of size scales from the micro-scale grains to large-scale faults extending over tens of kilometres (Bésuelle and Rudnicki 2004). The typical deformation bands can be characterised as dilation bands, shear bands, compaction bands, or a combination of several band types, where these strain localisation bands are always associated with instability phenomena (Aydin et al. 2006; Fossen et al. 2007). Previous work on temperature sensitivity in rocks focused on thermal pressurisation of the pore fluids and solid phase, resulting in inelastic deformation inside a fault zone (Ghabezloo et al. 2009; Hu et al. 2020; Kümpel 1991; Regenauer-Lieb et al. 2020; Rice 2006; Sulem et al. 2007). This effect is unlikely to play a significant role in highly porous carbonates due to the inherent high permeability. It was also reported that bulk, pore, and rock-solid compressibility decrease with increasing temperature (Somerton 1992). Temperature can increase and activate chemical reactions such as mineral dehydration, carbonate decomposition, and dissolution or precipitation, which control the deformation bands' initiation and evolution. Heap et al. (2009) reported that a moderated temperature increase from 20 to 75 °C could enhance the rate of stress corrosion cracking, thus reducing the short-term strength and time-dependent creep behaviour of three sandstones. However, a few studies focus on low-temperature carbonates' behaviour, especially for highly porous carbonates stable at low to an intermediate depth in the crust, such as the Mount Gambier limestone in South Australia. Most laboratory studies on such carbonate rocks have focused on ambient temperatures, and the experimental data on the changes in transport properties that accompany deformation are scarce. This is especially the case for understanding the micro-scale phenomena driving the macro-scale observations.

### 1.2 Instabilities and Micro-deformation Mechanisms in Carbonate Reservoir Rocks

Shear bands are the most common deformation bands described in the geological literature, dominated by shear displacement with or without some additional compaction or dilation processes. Shear bands play a significant role in many engineering structures failures, including earthquakes, landslides, and slope instabilities (Fossen et al. 2018; Sulem and Stefanou 2016; Tondi et al. 2006). On the other hand, the formation of compaction bands corresponds to a tabular structure of localised compressive deformation that forms perpendicular to the maximum compressive principal stress without obvious shear strain (Charalampidou et al. 2011; Issen and Rudnicki 2000; Olsson 1999). Compaction bands are usually characterised by a significant pore collapse inducing permeability reduction in the direction perpendicular to the compaction bands, which controls the fluid flow in the reservoir rocks.

Compaction bands were first reported through field observation in Jurassic Aztec sandstone of south-eastern Nevada (Hill 1993) and later reported in other field-based studies (Mollema and Antonellini 1996; Rustichelli et al. 2012). Tondi et al. (2006) and Rustichelli et al. (2012) reported narrow compaction bands which oriented oblique and parallel to bedding in naturally deformed carbonates. In addition to field observations, compaction bands have been reported in laboratory experiments (Baud et al. 2015; Baxevanis et al. 2006; Han et al. 2013; Leuthold et al. 2021; Oka et al. 2006; Tembe et al. 2008; Vajdova and Wong 2003) and have been simulated in numerical–theoretical studies (Croize et al. 2013; Das et al. 2011, 2013; Issen and Rudnicki 2001; Olsson 1999; Shahin et al. 2020; Sternlof et al. 2005). The controlled laboratory experiments of formation of compaction and shear bands at different temperatures, confining pressures, and type and pressure of pore fluids (solely or coupled) have been conducted on siliciclastic rocks to large extent (Baud et al. 2000; Heap et al. 2009; Jasinski et al. 2015; Pons et al. 2011; Wong et al. 1997). However, such experiments on carbonates are somewhat limited. Also, the complex mineralogy and microstructure of the carbonate rocks (e.g., mineralogy, deposition, and diagenesis) (Rashid et al. 2017) make their coupled behaviour further complex (Abdallah et al. 2021; Cilona et al. 2014; Louis et al. 2009). Besides the internal characteristics of the carbonates, the coexistence of many external conditions such as stress, type, and pressure of pore fluid and temperature are hypothesized to play a significant role in controlling localised deformation. More importantly, it is known that such drivers (stress,

temperature, chemical reaction, and pore pressure) are tightly coupled, and if a particular process(es) is of interest, the other driver effects should be isolated.

The type of pore fluid, its potential chemical reaction, and the effect of such chemical reaction on specimen's properties have also been shown to affect the deformation bands in porous rocks. Water, a common pore fluid and commonly used as injection fluid for enhanced oil recovery (EOR) objectives, has been studied extensively. The reason behind the water-weakening effect relies on many possible mechanisms. For instance, when water exits as pore fluids, it tends to embrittle rock by pressurisation and lubrication (Anderson 1981; Violay et al. 2015; Violay et al. 2014). It can also decrease rock minerals' surface energy and drop the friction coefficient, promoting subcritical crack growth and stress corrosion (Atkinson 1984; Baud et al. 2000; Brantut et al. 2013; Kodama et al. 2013; Sulem and Stefanou 2016). The same mechanism was also hypothesized to explain the water-weakening effect of carbonate rocks (Baud et al. 2009; Nicolas et al. 2016). Ciantia et al. (2015) presented a micro-scale mechanism of the water-weakening effect on the decrease of rock strength and introduced three different water-weakening processes of carbonates, including (1) short-term depositional bonds destroyed debonding, which is related to the calcite powder that falls into suspension during water saturation; (2) long-term diagenetic bonds dissolved debonding which is affected by long-term dissolution processes; and (3) grain dissolution process which involving the grains, and starting with long-term dissolution simultaneously. More recently, Cai et al. (2019) reported that the water-weakening effect of rocks depends on the porosity and the mineralogy, especially the proportion of quartz and swelling clays. Besides the chemical reaction effect on the formation of compaction bands, the thermomechanical and thermo-hydromechanical (coupled thermal-pore pressure–stress) effects on compaction bands, especially in carbonate rocks (limestone), is scarce, requiring further research to shed light on the involved processes. Understanding the effect of temperature on the formation of compaction bands is particularly important for geological-scale investigation involving higher temperature conditions.

In this study, we therefore present a systematic micro–macro-scale investigation of thermomechanical and thermo-hydromechanical effects on the formation and evolution of compaction bands in highly porous limestone (~ 50% porosity Mount Gambier limestone). To investigate the thermomechanical and thermo-hydromechanical behaviours of the limestone samples, dry (helium saturated) and purified kerosene were used (e.g. Baxevanis et al. 2006; Cerasi and Walle 2016), respectively. To shed light on the micro-scale mechanisms, we used our newly developed X-ray transparent hydromechanical triaxial cell (Roshan et al. 2019) where the limestone specimens were scanned at confining pressures of 5 MPa with 25 °C, 50 °C and 80 °C temperatures. Note that the entire analysed temperature range shows sharp stress drops, and the experiment is therefore entirely performed in what is commonly understood as the brittle regime. However, we focus in the present manuscript on the micro-scale mechanisms and classify the brittle and quasi-ductile response of the material at such microscopic level where brittle creep is here classified as a micro-scale ductile response. We analysed the time-lapse monitoring of external fluid pressure, mechanical load, and strain in relation to the radiographs and the 3D-CT reconstructions. This allowed us to link the macroscopic constraints to the microscopic response of the investigated limestone.

## 2 Experimental Methodology

### 2.1 Rock Material and Sample Preparation

The triaxial experiments were performed on Mount Gambier limestone retrieved from the Gambier Embayment of Otway, the basin of Paleogene–Neogene age in southern South Australia (Bourman et al. 2016). Mt Gambier limestone is a highly porous (~ 50% porosity) fossiliferous carbonate that originated from extensive colonies of Bryozoa (or lace coral) that flourished on an open-marine shelf, formed over 30 million years ago. The sample consists of 96% calcite and has a small contribution of quartz, magnesite, and magnetite (accounting for the remaining 4%) from X-ray diffraction (XRD) analysis. Chen et al. (2020b) reported that the Mt Gambier limestone has been characterised as a dual-porosity profile from the mercury intrusion capillary pressure measurement (MICP): macro-pores ranging from 10 to 200 µm and nano-micro-pores ranging from 0.1 to 5 µm. The average porosity of the sample from MICP measurement and helium porosimetry was obtained as ~ 50% porosity.

Cylindrical cores with 12.7 mm diameter were drilled from the same block. Both sides were then carefully ground to flat and parallel surfaces with 0.02 mm accuracy to a final length of 20 mm. This specimen size and geometry are necessary to enable X-ray micro-computed tomography (XRCT) imaging. The X-ray transparent triaxial testing allowed the full-field XRCT measurements with sufficiently high resolution. For limiting the moisture effect, all the specimens were placed in a vacuum oven, dried at 110 °C for 48 h, and the temperature was then reduced to room temperature for another 24 h before conducting the experiments.

For thermo-mechanical testing, helium was used as pore fluid, and for thermo-hydromechanical testing, purified kerosene was used as pore fluid instead of water. It is noted that no significant reaction between helium or kerosene and calcite is reported (Karkush et al. 2013). In dry experiments, the specimens placed in the triaxial system was vacuumed, and helium was injected from the top platen into the specimen;

a digital gas pressure regulator was used to control the inlet pressure constant. To ensure that the specimens are saturated with kerosene, dry specimens were first placed in a desiccator at a vacuum of 1 Torr for 24 h at room temperature. After that, the kerosene was gradually injected into the vessel's bottom until the specimens were filled with kerosene. Complete saturation (> 95%) was verified by weighing the specimen for 2 weeks.

## 2.2 Thermo-hydromechanical Experiments

Simultaneous triaxial testing and XRCT scanning on the Mount Gambier limestone specimens were conducted using an X-ray transparent triaxial deformation apparatus (Chen et al. 2020b; Roshan et al. 2019). A servo-controlled loading frame was used for all the experiments, and an axial displacement of $3 \times 10^{-3}$ mm/s was set (corresponding to a nominal strain rate of $1.5 \times 10^{-4}$ $s^{-1}$). Axial displacement data were logged by the linear variable differential transducer (LVDT) with a sampling rate of 0.1 $s^{-1}$ (10 Hz). Axial load was logged externally by a high precision disk load cell (LPX-1000) with an accuracy of ± 0.001 kN.

The confining pressure is $P_c = \sigma_2 = \sigma_3$ and the pore pressure $P_p$. We denote the maximum and minimum compressive stress by $\sigma_1$ and $\sigma_3$, respectively. Also, the differential stress is defined by $q = \sigma_1 - \sigma_3$ and the effective mean stress is defined as $p = (\sigma_1 + 2\sigma_3)/3 - P_p$. The compressive stress and strain are considered positive. According to the previous study on Mount Gambier limestone, the confining pressure of 5.0 MPa was used to trigger the pure compaction bands (Chen et al. 2020b).

Two sets of experiments were conducted to investigate the thermomechanical and thermo-hydromechanical experiments. The thermomechanical experiments involved triaxial testing at 5.0 MPa confinement with helium at 25 °C, 50 °C, and 80 °C temperatures, and thermo-hydromechanical experiments consisted of triaxial testing at 5.0 MPa confinement with kerosene at the same temperatures. At least three repetitions were conducted for each test to capture the variability. The specimens were also CT scanned at several loading stages for each test that are discussed later in the next section.

A soap bubble gas flowmeter was used to measure the downstream gas flow rate (Skoczylas 2015) for helium saturated permeability. The inlet pressure of 0.5 psi (3.45 kPa) was chosen because of high Mount Gambier limestone permeability (in order of Darcy).

The temperature of the cell was elevated and controlled by the circulation of high-pressure and high-temperature confining fluid. The temperature-controlled distilled water was circulated with a Vindum pump (VP-3K-HC-T). This pump can work smoothly up to 3500 psi (24.13 MPa) and delivers oscillation-free flow rates ranging up to 97 ml/min. In our experiments, the pump was used as a flow rate-controlled mode to provide enough heat to warm up the specimen to the desired temperature (Fig. 15 in Appendix 1). A thermostat (Lauda Alpha A6) was used to control the hot water temperature (set as 95 °C) and to refill the Vindum pump. The water was collected from the outlet (back-pressure regulator). This

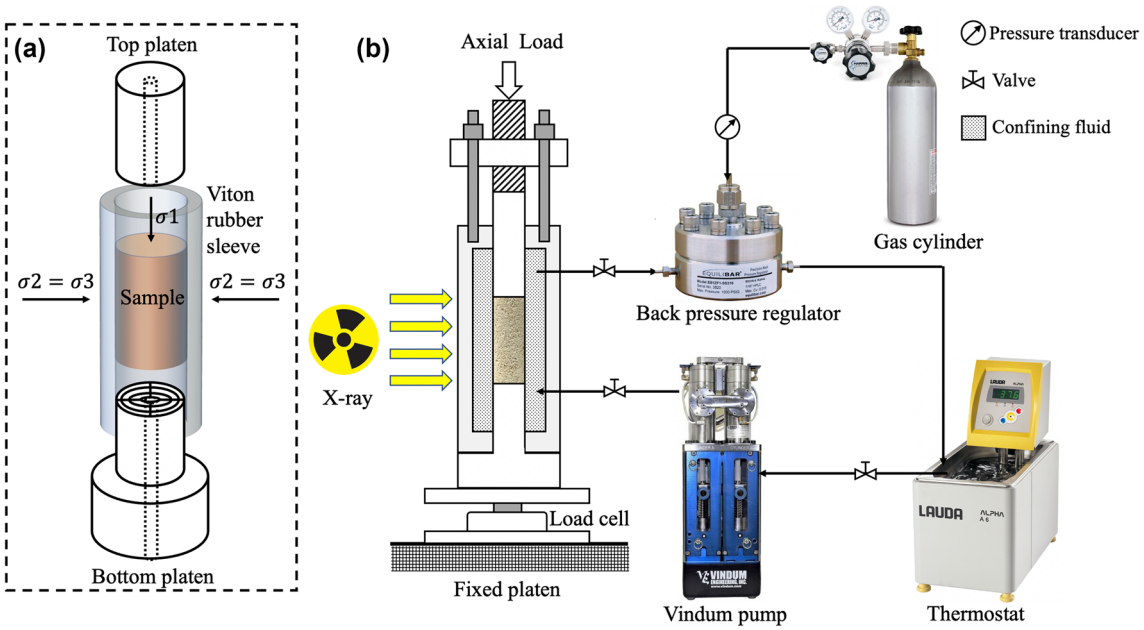


**Fig. 1** **a** The triaxial deformation apparatus's schematic shows the top and bottom platen pathways, allowing pore fluid injection and outflow. **b** The elevated-temperature experimental set-up

back-pressure regulator was connected to the air gas cylinder, and was used to control the confining pressure. The schematic figure of the elevated-temperature experimental set-up is presented in Fig. 1.

### 2.3 X-Ray CT Scanning and Image Processing

X-ray CT (XRCT) is a non-destructive imaging technique that quantifies an object's internal structure in 3D space (Arzilli et al. 2016; Lock et al. 2002; McBeck et al. 2020; Takano et al. 2015; Viggiani and Tengattini 2019). This technique was first used for medical purposes and later on widely used in engineering applications, including industrial use, geological investigation and material science. In this study, all the XRCT scans were conducted at the Tyree X-ray CT facility at the University of New South Wales, Sydney, Australia. The system has a GE Phoenix Nanofocus X-Ray Tube with a diamond window and a high-quality flatbed detector (3072 × 3072 pixels, 3.75 fps readout rate) which was designed to allow easy access and the ability to integrate complex flow experiments with the imaging system. The facility is built in a lead-lined room with excellent temperature and humidity control ($\Delta T < 0.5$ °C). In our study, the specimens were scanned in a circular trajectory with the setting of 100 kV, 120 µA, exposure time 0.6 s, three accumulations, 0.5 mm stainless steel filter, and 2880 projection per revolution. A resolution of 15.08 µm/voxel was obtained where the entire specimen was fitted in the field of view. The raw cone-beam X-ray projection data were reconstructed using the Katsevich algorithm (Kingston et al. 2016; Sheppard et al. 2014; Varslot et al. 2010).

In our study, time-lapse X-ray CT imaging was acquired on four specimens during their deformation at different conditions: MG-D25: helium saturated at 25 °C; MG-K25: kerosene saturated at 25 °C; MG-D80: helium saturated at 80 °C; MG-K80: kerosene saturated at 80 °C. The rest of the specimens were conducted at the same condition without X-ray CT to verify the repeatability. Before the experiment, each specimen was first scanned within the cell at unconfined conditions. After that, the specimens were loaded isotropically to 5.0 MPa stress, and triaxial loading was then applied to different axial strain levels while acquiring new series of tomographic images. All the experiments were conducted up to ~ 10% axial strain with five scans at different axial strain levels, while the static load (both axial and radial) is maintained during the scan. Each scan took 1.5 h to have sufficient time to obtain a resolution of 15.08 µm/voxel. During the 1.5 h scan, the potential of creep could occur; however, it was negligible in our measurements. This is because any creep would have caused failure of the reconstruction algorithm of CT raw images which relies on recognising features in the immediate vicinity of the previous scan 1.5 h prior.

After X-ray CT scanning, the image processing was conducted using the Mango software developed by the Australian National University. Mango is a powerful tool for parallel segmentation and network generation and the pre- and post-processing and analysis of associated data. The image processing workflow includes image cropping, edge enhancement, noise reduction, beam hardening correction, intensity calibration, and segmentation. For our time-lapsed X-ray CT images, intensity calibration and image registration were additionally performed. This is an essential part

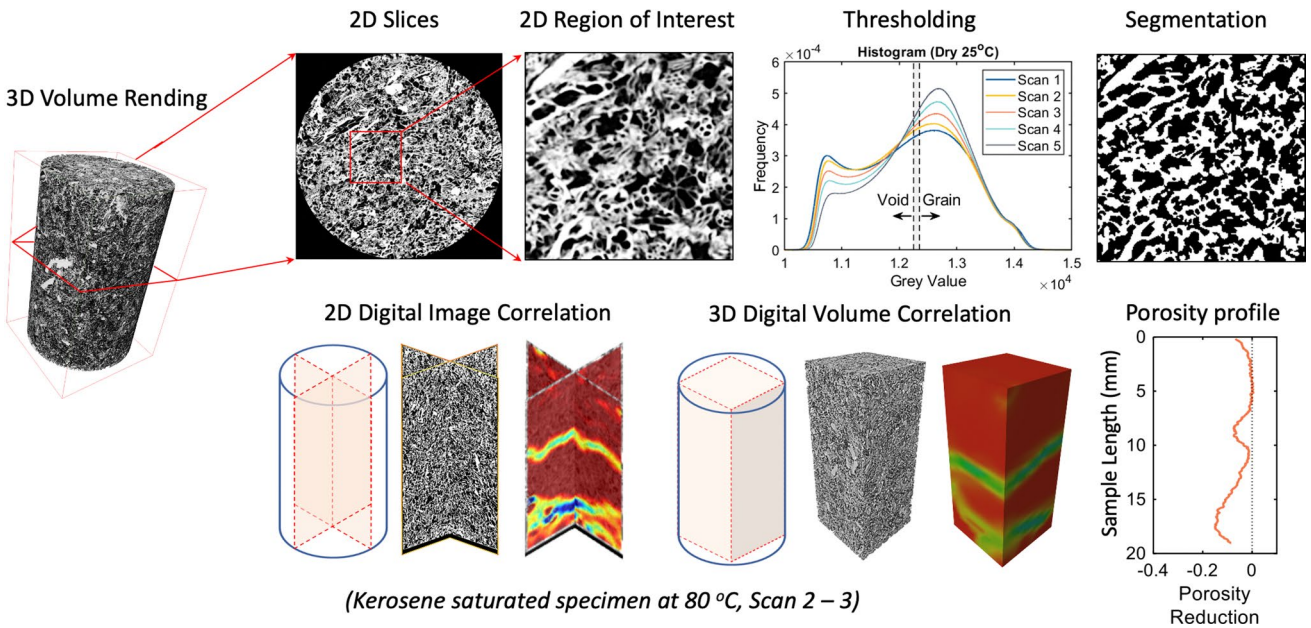


**Fig. 2** A simple workflow of X-ray CT image processing and further digital image analysis

of analysing a series of X-ray CT images of the specimen at different deformation stages (Fig. 2). Details on image registration and digital image correlation method for analysis can be found in Appendix 2.

## 3 Results

### 3.1 Thermo-hydromechanical Behaviour

#### 3.1.1 Helium Saturated Specimens

Figure 3a–c shows the stress–strain response of helium saturated specimens deformed at three temperatures (25 °C, 50 °C, and 80 °C). Four stage of stress–strain response is observed from the figure including Stage 1 where the stress–strain curve shows a short nonlinear response indicating the closure of pre-existing cracks and end-surface effects due to platen engagement (Renner and Rummel 1996; Walsh 1965). Stage 2 exhibits the linear elasticity until the yield point, followed by Stage 3, where the stress–strain relationship diverges from the linear relationship until the peak point. The beginning of the unstable cracking starts in this stage (Xue et al. 2014). At Stage 4, strain-softening, hardening, and pore collapse are observed (Bieniawski 1967; Eberhardt et al. 1999; Zhou et al. 2018).

Previous studies reported that the pressure drops are linked to nucleation and propagation of compaction bands (Baud et al. 2004; Chen et al. 2020b; Das et al. 2013), meaning that more compaction bands are nucleated and developed with an increase in temperature. The average strength of the rock reduces with increasing temperature, due to failure by a thermal weakening of the structure and thermally induced stresses hence lowering the strength by triggering more collapse of the pores (Mahmutoglu 1998; Sengun 2014). This will be further discussed in Sect. 3.2.

#### 3.1.2 Kerosene Saturated Specimens

To find out the effect of the pore fluid type on the formation of compaction bands, purified kerosene was used as pore fluid instead of helium. After immersing the specimen in kerosene through the vacuum desiccator, additional kerosene was slowly injected from the bottom port at a low constant flow rate: 3 ml/min to ensure full saturation of pores before the experiments. The same temperatures (25 °C, 50 °C, and 80 °C) as in the helium experiments were used. As shown in Fig. 3d–f, the stress–strain response and its temperature dependency show similar trends to helium saturated

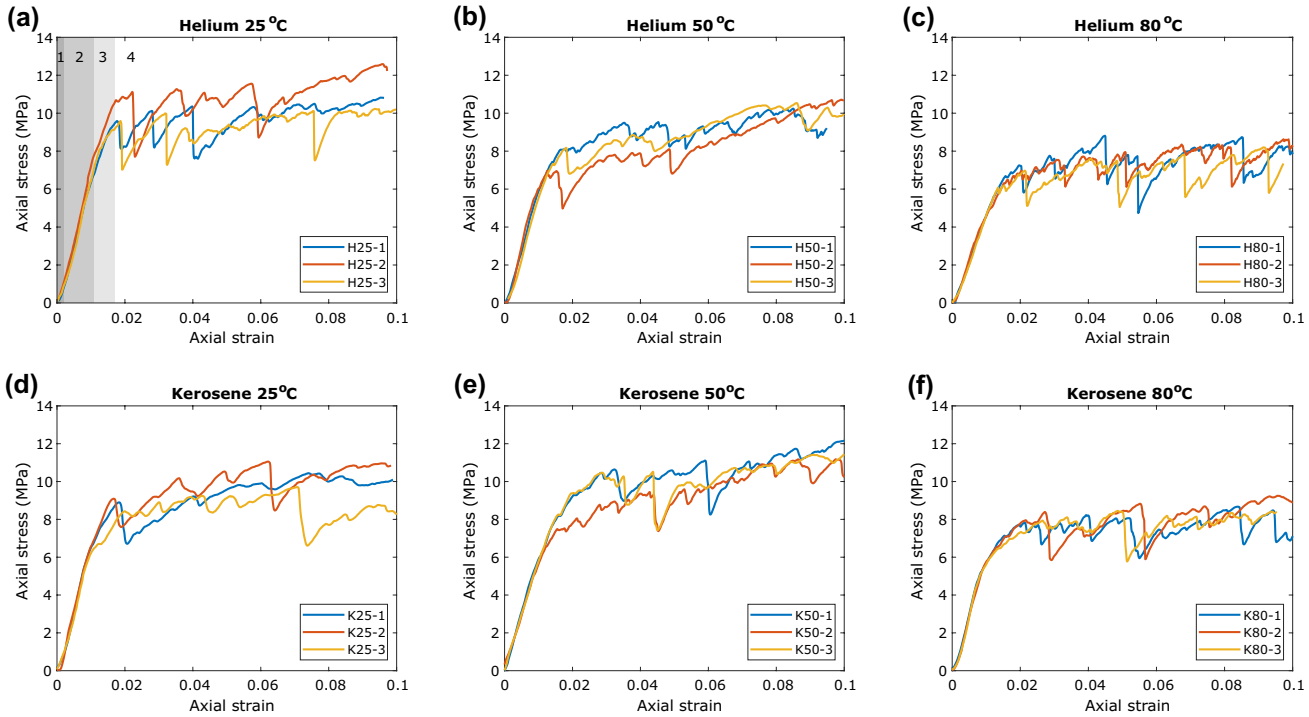


**Fig. 3** Axial stress versus axial strain for specimens deformed at **a** 25 °C, dry condition, **b** 50 °C at dry condition, **c** 80 °C at dry condition, **d** 25 °C with kerosene, **e** 50 °C with kerosene, and **f** 80 °C with kerosene. In each condition, three experiments were performed to assess the repeatability. Also, the stages of 1, 2, 3, and 4 on the **a** refer to the closing of pre-existing cracks, linear elasticity, divergence from the linear relationship, and strain softening and hardening, respectively

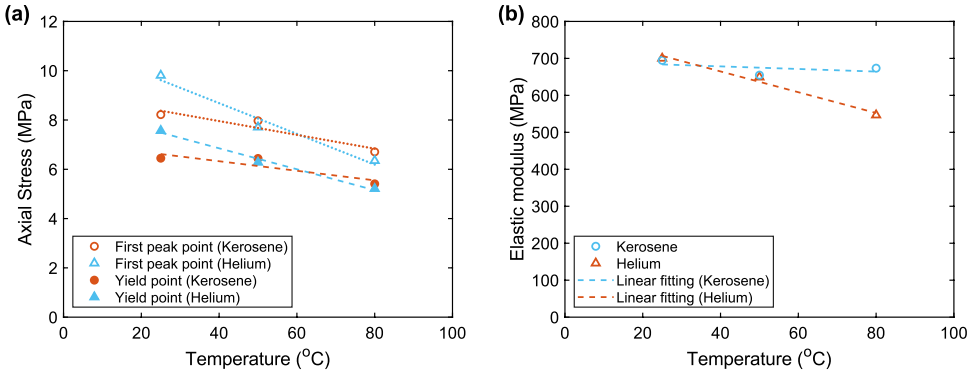


**Fig. 4** **a** Axial stress at first peak point and yield point versus temperature plot, and the dotted lines and dashed lines are linear fittings of peak stress and yield stress; **b** the elastic modulus for isotropic loading (< 5 MPa) before first yield as a function of temperature when saturated with kerosene and helium, respectively

specimens. Figure 4a shows the trends of the average stress at the first peak point and yield point with temperature for the experiments presented in Fig. 3. The value of axial stress at yield point and first peak point decreases in both helium and kerosene saturated conditions with a temperature increase from 25 to 80 °C. This temperature-sensitive trend was more pronounced for helium saturated specimens than kerosene saturated specimens. The average elastic modulus of helium and kerosene saturated specimens is plotted as a function of temperature in Fig. 4b.

## 3.2 Temperature-Dependent Micro-structural Alteration

To acquire a detailed map of the internal structure, the microstructural analyses were performed on four specimens, helium saturated condition at 25 and 80 °C, and kerosene saturated condition at 25 and 80 °C, using full-length 3D X-ray computed tomography. Figure 5 shows the stress–strain response of four tests with X-ray CT scanning, where each time-lapse experiment had five scans from 0% (undeformed) up to ~ 10% axial strain marked as S1–S5 in Fig. 5.

Digital image correlation analysis was performed on each specimen to track the initiation and evolution of localised compaction bands during the experiments at specified conditions. In our study, an open-source 2D-DIC code, Ncorr

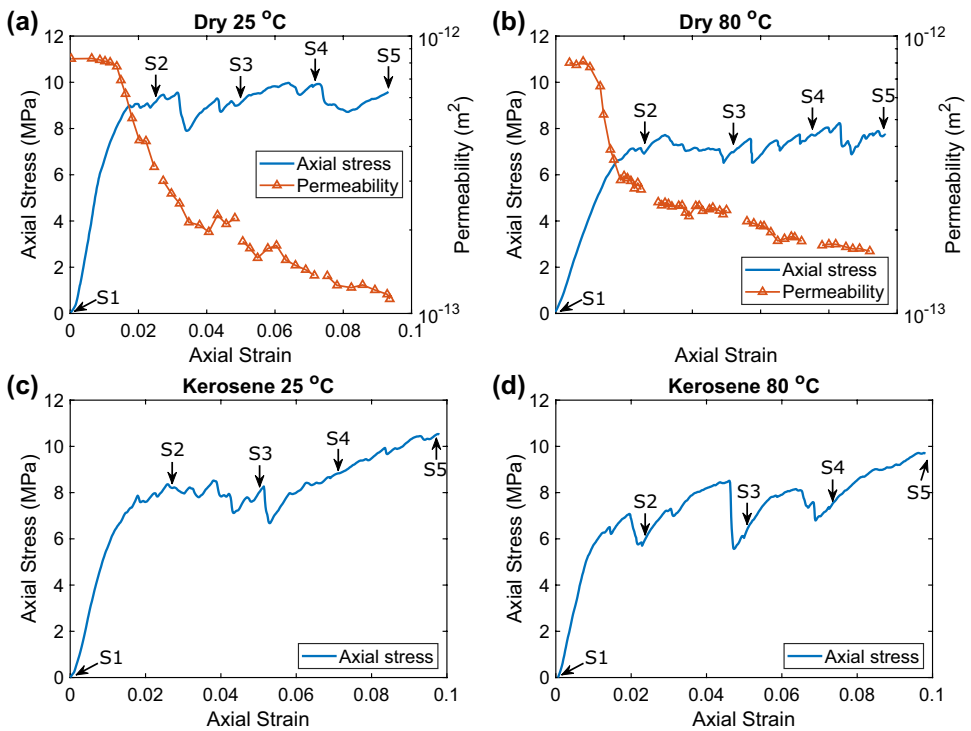


**Fig. 5** The axial stress–strain response of **a** specimen MG-D25, **b** specimen-D80, **c** specimen MG-K25, and **d** specimen MG-K80. S1–S5 indicates the number of scans at different axial strain levels. The permeability evolution curve in helium saturated samples is plotted in **a** and **b** using the Klinkenberg correction

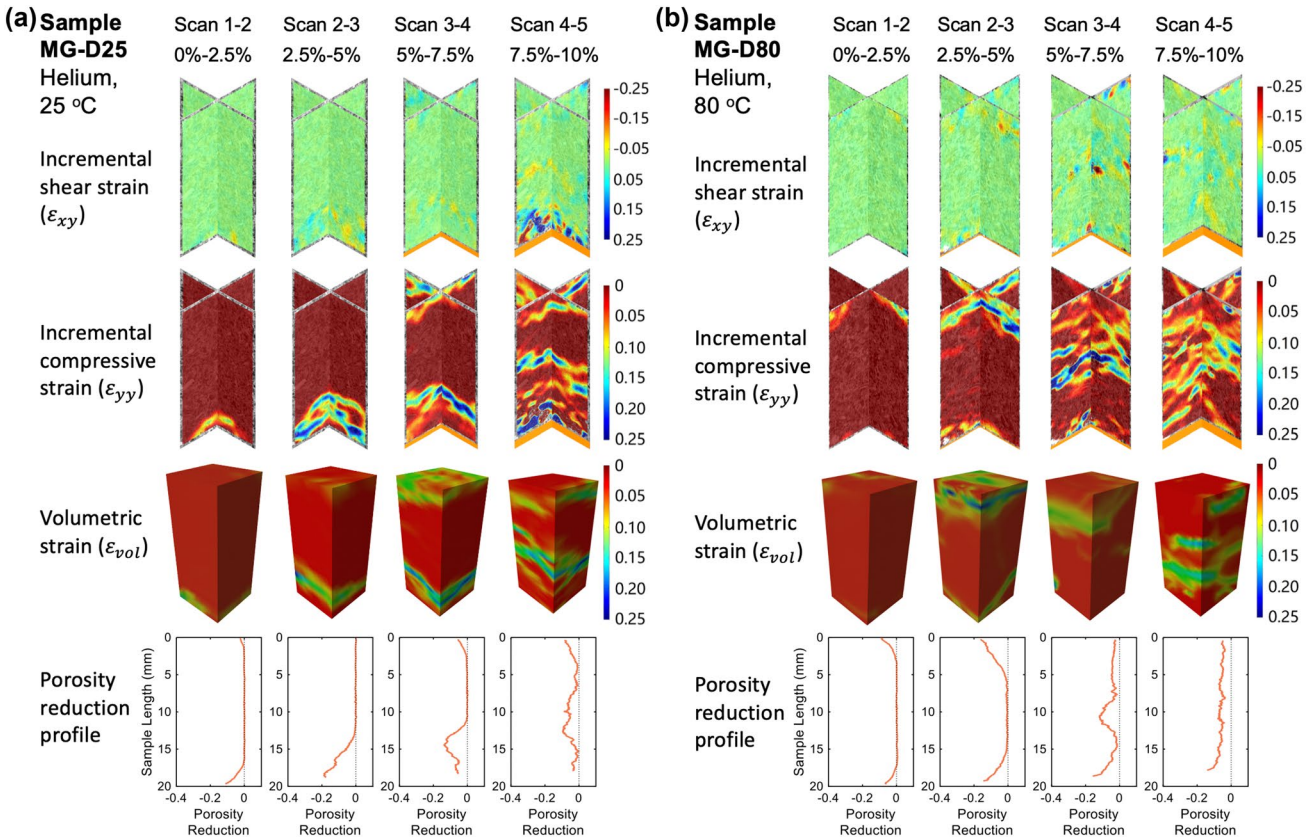


**Fig. 6** From top to bottom; the 2D incremental shear strain, 2D incremental compressive strain, 3D volumetric strain, and porosity reduction profile on **a** specimen MG-D25 (dry 25 °C) and **b** specimen MG-D80 (dry 80 °C)

(Blaber et al. 2015), was used to analyse the localisation and propagation of compaction bands over full-length 2D images as previously mentioned. We show two cross-section tomography planes (*XZ* and *YZ* planes) for 2D analysis. To assess the displacements and strain measurements within a sequence of tomographic volume images of a 3D subset, digital volume correlation (DVC) was additionally performed using Avizo 9.0 (Thermo Fisher Scientific). The contrast patterns were tracked from the reference tomography to the deformed state. Figures 6 and 7 represent 2D shear and compressive strain on two representative tomograph slices. The figures also show a 3D volumetric strain map on a maximum cuboid that was cut from the cylindrical specimen as well as porosity profile reduction between each scan for helium and kerosene saturated specimens at two different temperatures (25 and 80 °C), respectively. The first X-ray CT scan was acquired at 0% axial strain, followed by the second scan at 2.5% axial strain, which is higher than the yield point (1.5–2%).

Comparing Figs. 6 and 7 for helium and kerosene saturated specimens show some distinct differences. It is seen from Figs. 6 and 7 that the specimens saturated by helium at both low and high temperatures experience less compaction band formation than that of kerosene saturated specimens. To confirm this observation, we plot the overall porosity profile of the specimens extracted from segmented tomography images for both helium and kerosene saturated specimens at low and high temperatures, respectively (Figs. 8 and 9). It is noted that porosity extracted from images will have an accuracy limitation to image voxel resolution (15.08 µm). The porosity profile across the specimens proves the point observed from DIC–DVC analysis on the formation of compaction bands. These figures clearly show that kerosene saturated specimens undergo more significant pore collapse and associated damage (reduction in porosity) than the helium saturated specimens. For a more detailed investigation of this point, we extracted the radial and axial strains for both helium and kerosene saturated specimens at low and high temperatures from XRCT images at different measurement points and plotted them versus axial stress (Fig. 16 in Appendix 3). The figure shows that the helium saturated specimen develops a higher radial strain than the kerosene saturated specimen at both temperatures. We therefore conclude that the compression of the kerosene saturated specimen is accommodated by a higher degree of pore collapse thus reducing the radial strain upon compression. We

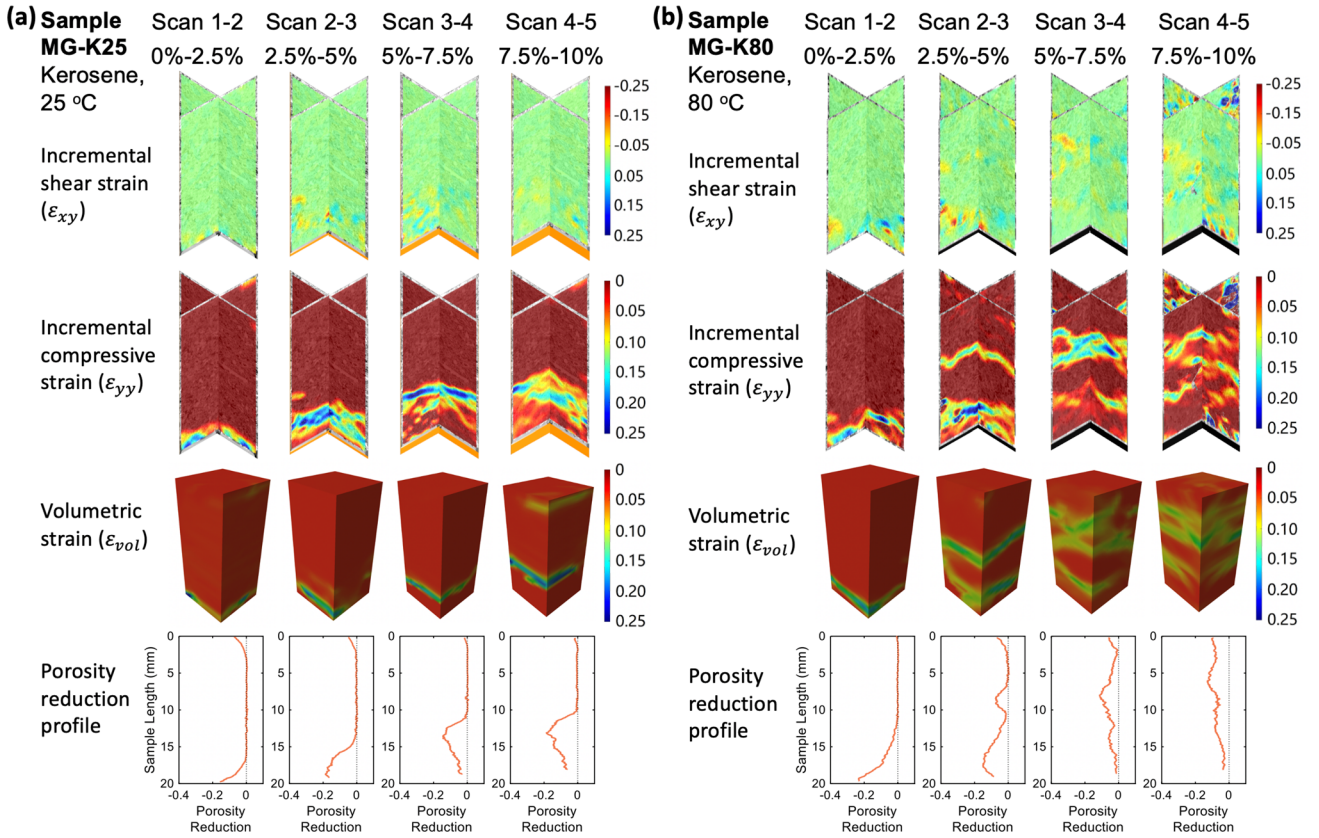


**Fig. 7** From top to bottom; the 2D incremental shear strain, 2D incremental compressive strain, 3D volumetric strain, and porosity reduction profile on **a** specimen MG-K25 (kerosene 25 °C) and **b** specimen MG-K80 (kerosene 80 °C)

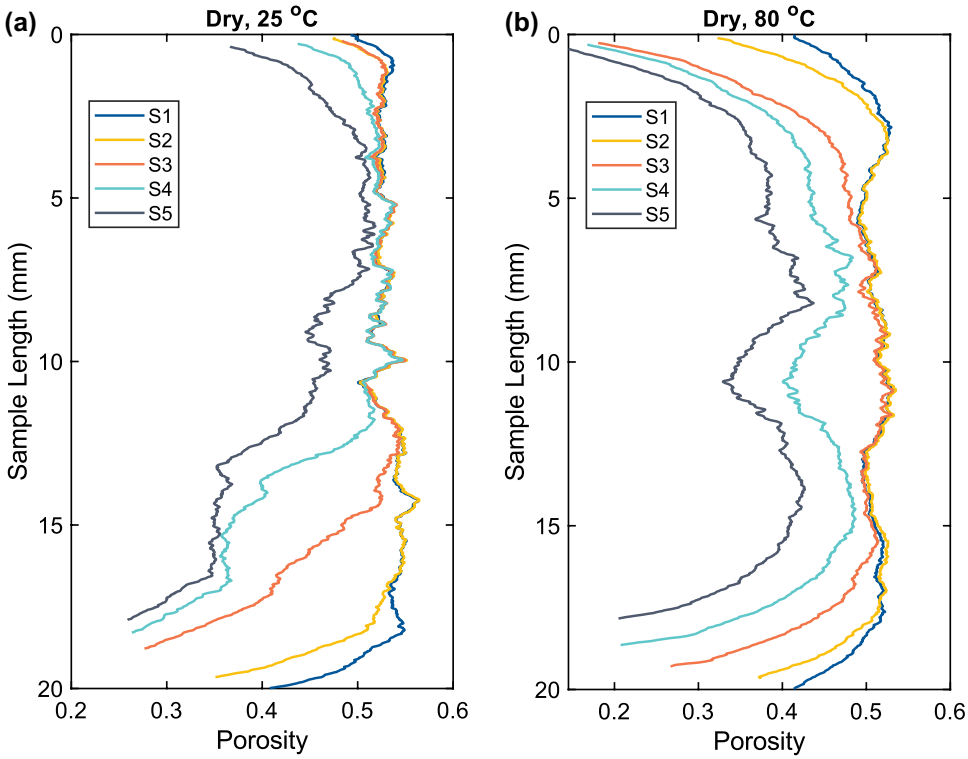


**Fig. 8** The porosity profile along $z$-direction of the specimens extracted from segmented images. **a** Specimen MG-D25 (dry 25 °C) and **b** specimen MG-D80 (dry 80 °C)

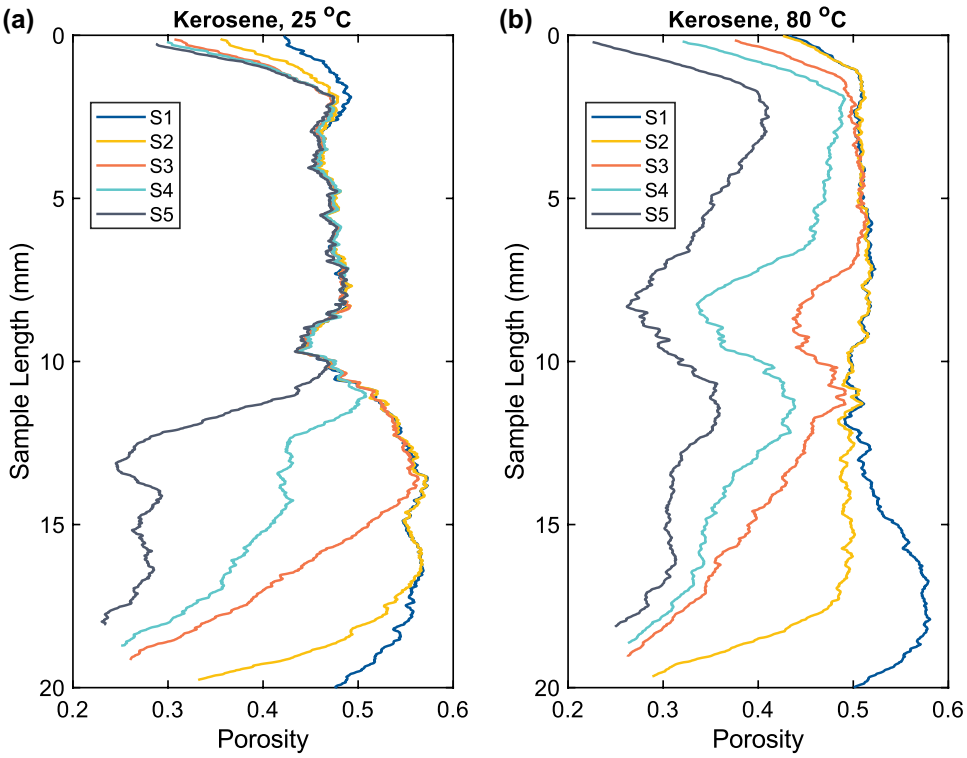


**Fig. 9** The porosity profile along *z*-direction of the specimens extracted from segmented images. **a** Specimen MG-K25 (kerosene 25 °C) and **b** specimen MG-K80 (kerosene 80 °C)

suggest that gas saturated matrix micro-pores accommodate a higher degree of elastic deformation prior to macro-pore collapse than the equivalent fluid-saturated matrix micro-pores. The difference in radial strain is interpreted as indirect evidence of the proposed role of compressibility of the gas-filled micro-pores in the matrix surrounding macro-pores.

### 3.3 Effect of Temperature on Permeability Evolution of Compaction Bands

Compaction bands have been reported to have a negative effect on fluid flow by creating a dramatic decrease in local porosity and permeability within the formed bands (Baxevanis et al. 2006; Fortin et al. 2005; Lenoir et al. 2010; Sternlof et al. 2006). In our study, sample permeabilities were measured on helium saturated specimens during the deformations where the X-ray CT imaging sheds light on the mechanism of permeability reduction due to formation of compaction bands in the presence of thermo-hydromechanical interaction. This technique offers a superior understanding of how permeability changes during the formation of compaction bands.

Helium gas was used for dry specimens as a working fluid, and continuous permeability measurements were carried out. The gas permeability is calculated by Darcy's equation for compressible fluids and further converted to a liquid permeability following the Klingenberg correction (Tanikawa and Shimamoto 2006). The permeability evolution as a function of axial strain is plotted in Fig. 5a, b, along with the stress–strain response of helium saturated specimens at 25 and 80 °C, respectively. The overall trend of permeability reduction has been previously reported, and the processes are discussed (Chen et al. 2020a). Both specimens tested under low and high temperatures show similar initial permeability. At 25 °C condition, the permeability reduced from $8.3\times10^{-13}$ to $1.13\times10^{-13}$ m$^2$; at 80 °C, the permeability reduced from $8.2\times10^{-13}$ to $1.77\times10^{-13}$ m$^2$. However, with the increase of axial load, the reduction in permeability becomes highlighted for the low-temperature specimen compared to the high temperature one. This is especially the case once the 5% axial strain is passed. The permeability result contrasts with the DIC analysis performed on XRCT images which shows that the specimen experiences a much higher degree of compaction and compaction band development at a higher temperature. We will discuss this in the next section.

## 4 Discussion

We presented our analysis on highly porous carbonate where we systematically investigated the effect of pore fluid type and temperature on the micro-mechanisms of failure, localisation behaviour, and overall strength evolution. Insights into micromechanical aspects were gained indirectly through

DIC/DVC analyses of X-ray CT scans and direct radiographs observations.

## 4.1 Pore Fluid Effect

### 4.1.1 Effect of Dual Porosity and Drainage Conditions

Experiments performed with a chemically inert fluid showed only a slight effect of fluid type on yield stress in the high-temperature regime but a more highlighted effect at low temperatures. The results clearly showed that experiments performed with helium have higher yield stress than experiments where specimens were saturated with kerosene as a pore fluid. An obvious candidate for the effect would be chemical weakening. However, the effect of chemical reactions of kerosene with the carbonate matrix can be ruled out as there is no significant reaction reported in the literature (Karkush et al. 2013).

The limestone sample has a unique dual pore size distribution with distinct clusters of micro-pores (~ 100 nm–5 µm) and macro-pores (~ 10–200 µm) (Chen et al. 2020b). The micro-pores are an integral part of the skeleton around the macro-pores and they therefore have a significant effect on mechanical matrix properties. The applied fluid pressure is low and drainage conditions are supported by the percolation network of the macro-pores for both kerosene and helium. We can speak of drained conditions for the macro-pores and the different effect of compressibility of fluid or gas does not play a role. The fluid/gas in the micro-pores of the skeleton, however, has to pass through narrow pore throats causing a deviation from the drained response. This near "undrained" response in drained testing condition is well documented for tight rocks such as shale where micro-pores dominate the pore structure (Roshan and Aghighi 2012; Roshan and Rahman 2011). Therefore, the restricted permeability in the micro-pores implies that the difference in compressibility of fluid versus gas can manifest itself in the experiment.

This near "undrained" response in specimens saturated with kerosene will have two distinct effects. First, due to partial support of the load by the liquid in micro-pores, one expects to see stiffening of the skeleton causing a slight increase in elastic modulus for the specimens saturated with kerosene compared to helium (Levy et al. 2000; Mavko et al. 2020). On the other hand, the increase in pressure in these micro-pores should lead to a reduction of the yield stress (Han et al. 2019; Robinson 1959). The strength reduction is well observed in the experiments with kerosene and helium at low temperatures, although the increase in elastic modulus is less apparent.

An interesting observation is that the elastic loading path at 80 °C shows a higher elastic modulus for kerosene than for helium, while the difference in yield stress vanishes (Fig. 4). The vanishing difference in yield stress is likely linked to a decrease in kerosene viscosity with temperature enabling it to escape the micropore under drained condition, thus leading to a minimal pore-pressure build-up in these micro-pores. The difference in elastic modulus is attributed to the temperature sensitivity of the elastic deformation that will thus be discussed in the temperature dependence section.

### 4.1.2 Effect of Reduction in Surface Energy

As previously mentioned, no chemical weakening such as calcite-pressure solution (Hellmann et al. 2002; Newman 1983; Plummer and Busenberg 1982) or corrosive deterioration (Atkinson 1984; Karner et al. 2005; Wiederhorn 1967) can be triggered by kerosene in our experiment. However, the important physico-chemical mechanism of surface energy reduction remains to be investigated. It is well known that the reduction in surface energy promotes the initiation and growth of micro-cracks (Griffith 1921). The surface energy of minerals is formed through interaction between the solid surface and exposed fluids (Siddiqui et al. 2019). In our study, we deal with kerosene and helium which should essentially have different surface energies with calcite minerals leading to different mechanical responses due to resultant crack propagation (Rostom et al. 2013; Zeng et al. 2020). To investigate the change in surface energy and its relation to sample weakening, we use the Griffith crack theory that provides a simple fracture mechanics model stating that fracture energy, $G$, is equal to the energy necessary to produce the two surfaces of a new fracture or twice the surface energy

$$G - 2\gamma_s^e = 0, \tag{1}$$

where $G$ is the mechanical energy and $\gamma_s^e$ is the surface energy of the solid in contact with a given environment. The lowering of the surface energy of the material can enhance crack propagation. Helium is an inert gas and will not induce any surface energy alteration; thus, we focus on kerosene. To investigate the kerosene effect on surface energy and potential weakening of the limestone sample, we choose to compare it with water that is known to have a severe effect on rock mechanical properties including calcite rich rocks (Lisabeth and Zhu 2015; Liteanu et al. 2013; Risnes et al. 2003, 2005; Røyne et al. 2011).

Contact angle measurement is an indirect technique to characterise the surface energy of a solid in presence of fluids (Siddiqui et al. 2019). The results of contact angle measured for water–calcite–air system and kerosene–calcite–air system are presented in Fig. 17 in Appendix, i.e., 20° and 5° for water and kerosene contact angles, respectively, after stabilisation. Knowing that water–air and kerosene–air surface energies are 0.0728 N/m at 25 °C (Lange and Dean 1967) and 0.0267 N/m at 25 °C (Landry et al. 2011), respectively, one can calculate the difference in surface energy of

calcite–water and calcite–kerosene as shown in Appendix 4 (Link and Schlünder 1996). This calculation shows that the calcite surface energy with water is lower than kerosene. Knowing that the surface energy of minerals are lower when exposed to liquids compared to gases (Brunauer et al. 1956), we conclude that kerosene promotes less crack growth and fracture propagation than water, but it still contributes to a reduction in surface energy and promotes cracking higher than helium case. The reduction of the strength of specimens in low temperature (25 °C) is approximately 15% which is similar to Baxevanis et al.'s (2006) results. Compared with the experimental results using water as pore fluid, e.g., (Liteanu et al. 2013; Risnes et al. 2003), our results showed less strength reduction when using kerosene saturated specimens consistent with contact angle measurements. Overall, the weaker structure is experienced for specimen saturated by kerosene. This effect is strongly visible in formation of compaction bands and reduction of specimen porosity with kerosene (Figs. 8 and 9) at any temperature, although such effect is not very pronounced in the values of initial yield strength dominated by the heterogeneity of different samples.

## 4.2 The Role of Temperature

In the results chapter, we showed a systematic weakening in both helium and purified kerosene experiments when raising the temperature from 25 to 80 °C. The stress–strain response and its temperature dependency of helium and kerosene saturated experiments show similar trends. The average strength of the rock reduces with an increase in temperature (Fig. 3). An interesting observation is the effect of temperature on the near-elastic branch of the load curve. The helium saturated specimen showed a distinct temperature sensitivity with a systematic elastic modulus drop at a higher temperature.

In contrast, the elastic modulus in kerosene saturated specimen appeared to be slightly affected by a temperature change. The combination of temperature sensitivity of the carbonate matrix and near "undrained" response discussed before is the likely cause for this behaviour. While the carbonate matrix weakens with the increase in temperature (Sulem and Stefanou 2016; Wong et al. 2020; Yavuz et al. 2010), the undrained response of kerosene dominates the weakening effect of the matrix by temperature; thus, a lower drop in elastic modulus is observed in kerosene case compared to that of helium. It is, however, difficult to ascertain the exact roots of the weakening of the elastic modulus for the helium saturated specimens as the effect is not directly measurable and is modulated through the dynamics of matrix–pore interactions. In the following section, we will discuss the temperature effect on the yield phenomenon in further detail.

### 4.2.1 Helium Saturated Experiments

The comparison of the helium saturated experiments performed at lower and higher temperatures indicates a transition in deformation mode. From macroscopic observation, the strength of the specimens reduces with increasing temperatures from 25 to 80 °C. Similar results have been reported by Liteanu et al. (2013); a reduction in overall strength (approximately 2 MPa) has been observed when increasing the temperature from 25 to 80 °C at 5 MPa confining pressure using dry Maastrichtian chalk, which has similar composition and porosity to Mt Gambier limestone. More localised deformation features within the specimens can be seen from DIC and DVC analyses at a higher temperature (Fig. 6).

To find out the microstructural changes between lower (25 °C) and higher (80 °C) temperatures, a selected region of interest (ROI) window is shown in Fig. 10. The figure highlights the microstructure evolution in the leading compaction bands and undamaged matrix at Scan 2 (2.5% axial strain), Scan 3 (5% axial strain), and Scan 4 (7.5% axial strain). At lower temperature (25 °C), pore collapse happened within the compaction bands seen by tomographic observations as highlighted by the red dashed box in Fig. 11a. There is no pore collapse observed in the undamaged matrix (Fig. 11a–c). When increasing the axial strain from 2.5 to 7.5%, the main compaction band that nucleated from the lower boundary propagates towards the middle of the specimen as a wavefront (Fig. 11d, e).

We infer that the front-like propagation of damage of the specimen is controlled for the low-temperature experiments by rate dependence of the material. This rate dependence relies on the formation of new surfaces between the calcite grains for which there are many possible deformation mechanisms. We have not performed a microstructural analysis of the sub-micro-scale processes. However, from the literature, one of the possible candidates is calcite twinning. This low-temperature ductile effect triggers pervasive deformation (Rowe and Rutter 1990). Brittle mechanisms such as pore collapse, crack growth, and grain crushing are competing deformation mechanisms promoting localised deformation features that have a much faster dynamic response than the slow speed of propagation of the wavefront, which is controlled by the twinning reaction. The brittle mechanism presumably operates in conjunction with twinning. However, the macroscopic behaviour appears to be akin to a plastic deformation that affects the propagating front pervasively, while the remainder of the specimen remains intact. The low-temperature deformation mode has been encountered in many similar experiments and is called a "diffuse compaction band" (Louis et al. 2006; Tembe et al. 2006; Wang et al. 2008) which contrasts with the localised style of compaction encountered in the high-temperature experiments.

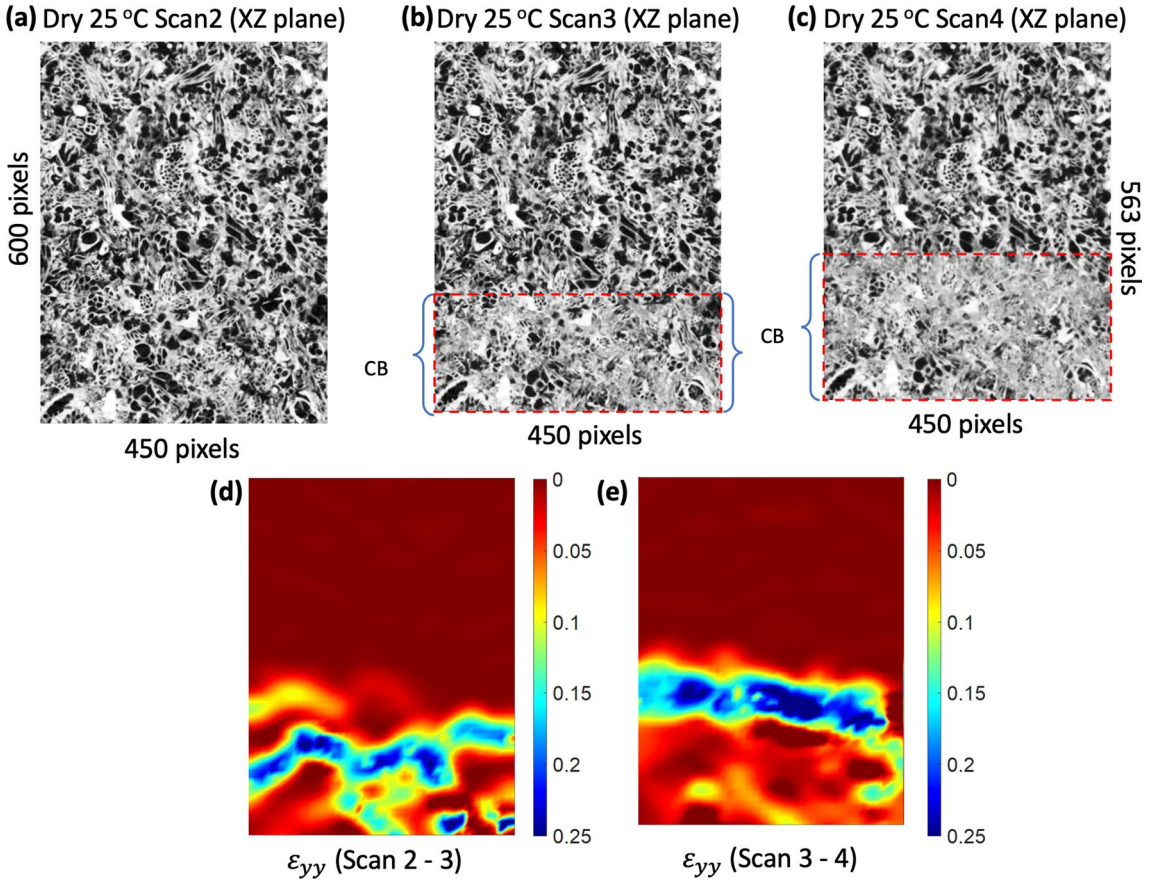


**Fig. 10** **a–c** Microscopic view of the ROI window cropped from the tomography slices (*XZ* plane) of specimen MG-D25 at scan 2, 3, and 4, respectively. The black colour represented the pores, and the grey colour indicates the grain (matrix). The red dashed box indicated the main compaction band. **d** and **e** are the $\varepsilon_{yy}$ strain map between Scan 2–3 and Scan 3–4, respectively

At a higher temperature (80 °C), we observe diffuse and highly localised deformation features (Fig. 11). The new observation at high temperature is the localised compaction band that starts at scan 2–3 in Fig. 5b at the top boundary, but does not propagate as a steady wavefront like the diffuse band but jumps towards the middle of the specimen. Brittle localised pore collapse or damage can be clearly identified in the otherwise undamaged matrix from Scan 3 onwards (Fig. 11), indicating that brittle deformation has a more prominent effect at higher temperatures. When zooming into the pore collapse of the smallest pores highlighted in the red box (Fig. 12), we can see that the weaker structures failed in random directions according to the weakest point of the structure itself (Fig. 12), and the broken pieces fall into the open pores as crushed rocks. At scan 4, the pore collapse of the small pores developed as a localised deformation band easily recognised from the strain map showing that the specimen failed in a more complex manner on different localised compaction bands. The behaviour of small pores collapse is different from the previously reported mechanism of discrete compaction bands in dry specimens (Chen et al. 2020a). The discrepancy between the dominance of diffuse compaction band growth versus localised features at higher temperatures experiments is a new observation that has not been reported in the literature before. The importance of the microcrystalline behaviour of the matrix in conjunction with the interaction of the pore filling fluids needs further explanations of the somewhat counterintuitive dominance of a brittle deformation mode at higher temperatures.

In the following, we attempt to find explanations for observing the promotion of brittle effects at a higher temperature. Circumstantial evidence for brittle deformation dominance at a higher temperature is that sample heterogeneity appears to be more important at controlling localisation features especially with the reduction in matrix strength. Another indirect evidence is the effect

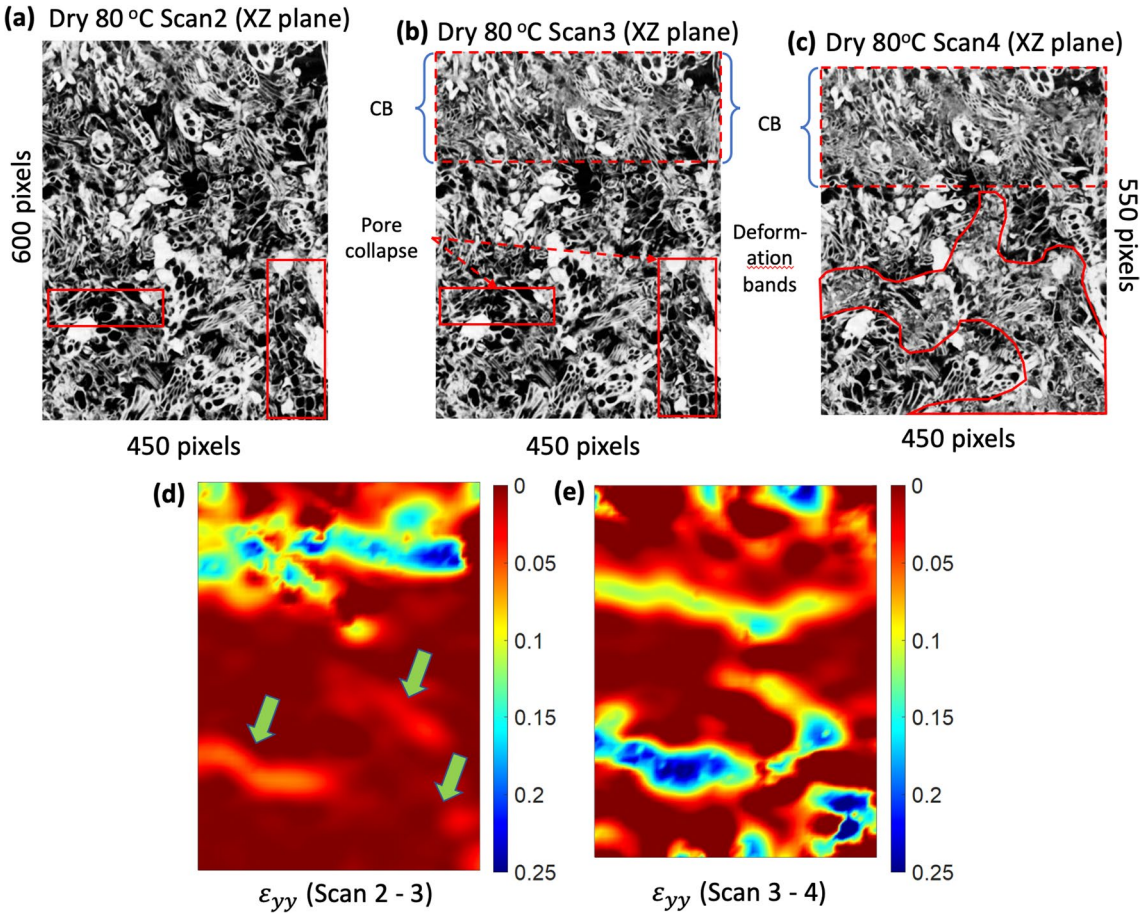


**Fig. 11** **a**–**c** Microscopic view of the ROI window cropped from the tomography slices (*XZ* plane) of specimen MG-D80 at Scan 2, 3, and 4, respectively. The black colour represents pores, and the grey colour indicates the grain (matrix). The red dashed box indicated the main compaction band, and the red solid line area indicated deformation features within the undamaged matrix. **d** and **e** are the $\varepsilon_{yy}$ strain map between Scan 2–3 and Scan 3–4, respectively (colour figure online)

of permeability reduction reported in Fig. 5a, b, showing that the low-temperature regime shows a higher reduction in permeability with strain. In contrast, the high-temperature experiments have a milder effect on permeability reduction. This is interpreted here through the pervasive destruction of fluid pathways in the low-temperature regime through the diffuse deformation bands contrasting to the smaller localised brittle damage zones from the higher temperature experiments. The transition from dominantly ductile at low temperatures (25 °C) to dominantly brittle at higher temperatures (80 °C) is also clearly illustrated in Figs. 11 and 12.

#### 4.2.2 Kerosene Saturated Experiments

A similar transition in deformation mode has been observed in kerosene saturated experiments. The overall reduction of the yield strength of the specimens from 25 to 80 °C is clear through the overall load curve (Fig. 3). Interestingly, although there is a strong difference in elastic behaviour, the yield strength of the helium saturated specimen compared to the kerosene saturated one shows similar values at high temperatures. At the low temperature, there is a marked difference in yield strength. Because the differences in yield strength between high and low temperatures are observed for all specimens, including those where the pores are filled with helium gas, we rule out the dominance of the surface tension effect on temperature. It is instead more likely that the difference is caused by the afore-documented transition in dominant deformation mode from a temperature-sensitive ductile deformation to a temperature-insensitive brittle deformation mode at high temperature.

The observation supports the interpretation of a transition in dominant micromechanical deformation mode that at lower temperatures, kerosene saturated specimens exhibit the same pervasive deformation mode as helium saturated ones. Similarly, both gaseous and fluid-saturated specimens

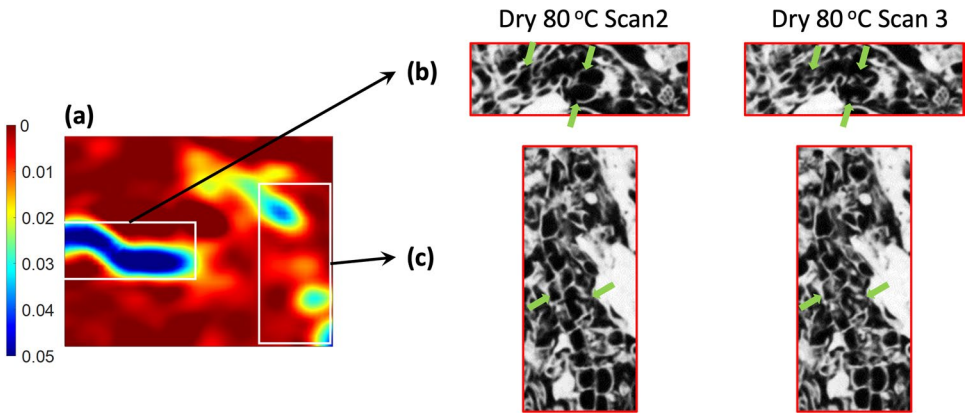


**Fig. 12** **a** The $\varepsilon_{yy}$ strain map between Scan 2–3 of specimen MG-D80 (narrowed colour range); **b** and **c** are details of two highlighted features of specimen MG-D80 at Scan 2 and Scan 3. Arrow pointed out the pore collapse along with the weakest structure

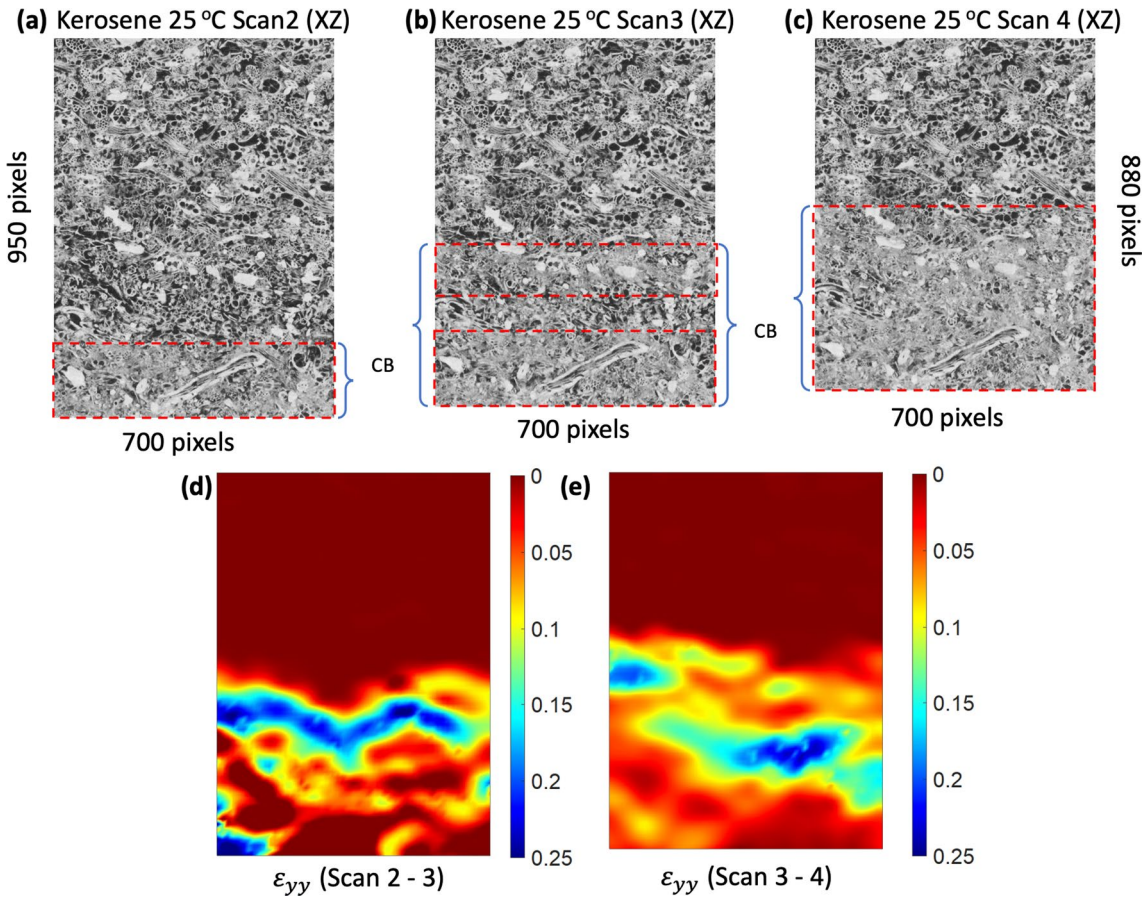


**Fig. 13** **a**–**c** Microscopic view of the ROI window cropped from the tomography slices (*XZ* plane) of specimen MG-K25 at scan 2, 3, and 4, respectively. The black colour represented the pores, and the grey colour indicates the grain (matrix). The red dashed box indicated the main compaction bands. **d** and **e** are the $\varepsilon_{yy}$ strain map between Scan 2–3 and Scan 3–4, respectively

show the same localised deformation features within the specimens, as seen from DIC and DVC analysis at a higher temperature (Fig. 7). A representative example of the prominent propagating wavefront of the diffuse compaction bands in both helium and kerosene cases is shown in Fig. 13.

This deformation mode is in stark contrast to the DIC map recorded at higher temperatures. Localised pore collapse becomes predominant, and individual pores collapse and crush to form coherent localised deformation features at higher axial strain (Fig. 14). A narrow compaction localisation is nucleated between Scan 2 to Scan 3, both seen in the tomography images and the strain map (Fig. 14b, d). The deformation bands are more evident in particular selected tomographic slices (Fig. 14c) than in the strain map

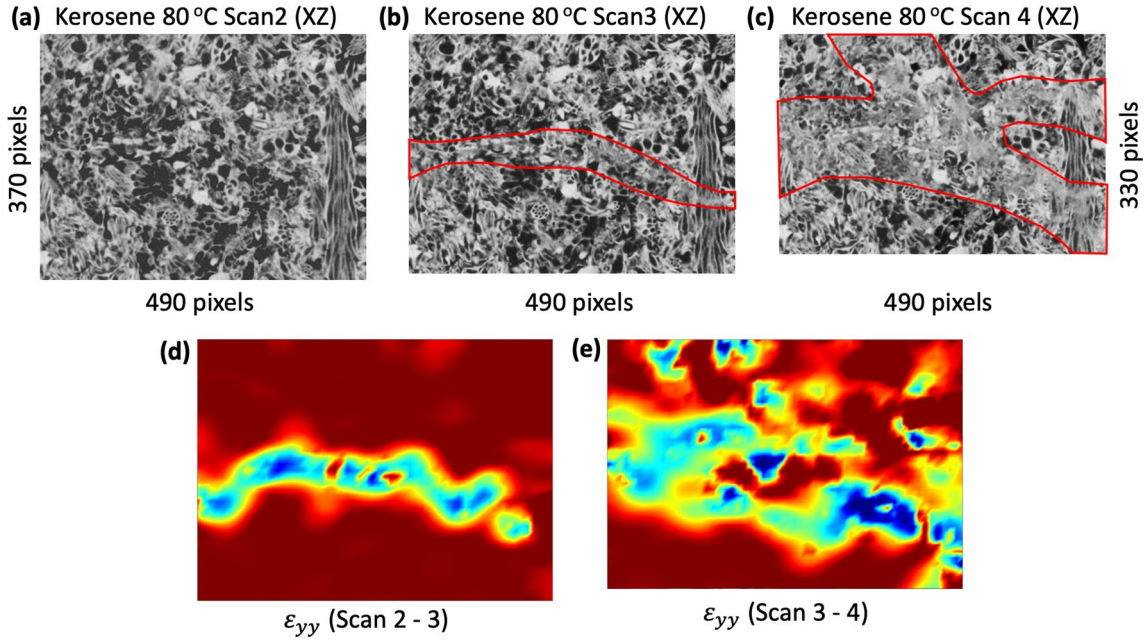


**Fig. 14** **a–c** Microscopic view of the ROI window cropped from the tomography slices (*XZ* plane) of specimen MG-K80 at scan 2, 3, and 4, respectively. The black colour represented the pores, and the grey colour indicates the grain (matrix). The red solid line area indicated the main deformation bands. **d** and **e** are the $\varepsilon_{yy}$ strain map between Scan 2–3 and Scan 3–4, respectively

(Fig. 14e). This is due to the high degree of localisation and the inability of the DIC algorithm to track the crushed calcite powder that fills the larger pores as reference points are vanishing.

In summary, our systematic comparison of the results from gaseous and fluid-saturated experiments shows that a pervasive ductile deformation mode dominates at a lower temperature and a localised brittle deformation mode at a higher temperature. We attribute this effect to two main reasons. The low-temperature ductile effect is rate controlled by calcite twinning, which is known to occur at room temperature (Friedman and Heard 1974; Guéguen and Boutéca 2004; Parlangeau et al. 2019; Turner et al. 1954). This effect controls the slow propagation of the main compaction bands from the boundary towards the middle of the specimen. At higher temperatures, the Peierls mechanism can be triggered, which shows little rate dependency and is called low-temperature plasticity (Sly et al. 2020). Although this mechanism is a ductile micro-mechanism, its viscous damping is very low due to the near-ideal plastic response. It, therefore, can assist or trigger the macroscopic brittle failure of the skeleton, assisted by the surface energy effect of the fluid phase.

Our new observations may alternatively be interpreted by a proposed temperature-sensitive mechanism proposed by earlier analyses. These report that moderate temperature changes can significantly affect the mechanical behaviour of deformation bands. Explanation in the literature (Ghabezloo et al. 2009; Kuempel et al. 2017; Lemos 2003; Renard et al. 2009) attributed the effect to changes in the stress-state affected by thermally induced pore-pressure changes, thus lowering the threshold for induced brittle damage. Yavuz et al. (2010) examined three different limestones: monomineralic rock (almost calcite), similar to Mt Gambier limestone used in our study. Dilation of calcite and compaction of grains has been observed when temperature increased to 100 °C; this compaction of grains resulted in an effective porosity decrease. Nicolas et al. (2016) reported that the temperature difference between 20 and 70 °C can result in shear-enhanced compaction triggered at lower confining pressure in dry Tavel limestone. However, we consider the temperature-sensitive pore-pressure effect to be negligible in our specimens. All mechanisms can co-occur, making it difficult to differentiate between thermally induced weakening through pore-pressure changes and alternative transitions in deformation behaviour of the solid matrix as suggested by us.

## 5 Conclusion

We have conducted a series of triaxial compression experiments on a highly porous Mt Gambier limestone and investigated the effect of pore fluids and temperature on mechanical behaviour. Concurrent compression tests with X-ray CT scans were used to offer a time-lapse evolution of the deformation localisations and digital image analysis, offering a

micro-structural observation under in-situ conditions. This study used an ideal thermo-hydro-poro-mechanical system to eliminate the chemical reaction, using purified kerosene and helium gas as pore fluids. Two novel fundamental observations were made:

1. We have observed that the yield stress of nominally inert gas (helium) saturated specimens is higher than the nominally inert liquid (purified kerosene) saturated specimens. Conversely, the elastic modulus was lower for the inert gas saturated specimens than inert fluid-saturated specimens. We attribute the effects to the near-undrained response of the sub-micro-scale pore system of the specimen.
2. A second important observation is a changeover from ostensibly ductile to a dominantly brittle deformation when raising the temperature. Regarding the core scale mechanical behaviour affected by moderate temperature change, our time-lapse experiment with X-ray CT tomography provided a microscopic view of structural alteration during compaction band formation. A transition in deformation mode was observed in both helium and kerosene saturated conditions when increasing the temperature from 25 to 80 °C. At lower temperature, we have observed wave-like propagation of compaction bands propagating from the boundary towards the specimen's middle. At high-temperature, pore collapse, shear or shear-enhanced compaction localisation and Mode 1 initial crack orientation indicate that brittle deformation has a more prominent effect at higher temperatures. In the low-temperature ductile regime, compaction bands' formation shows pervasive deformation with no visible damage or pore collapse in the undamaged matrix. The undamaged matrix remained the stress supporting structure, and all the pore collapse happened within the diffuse compaction regions (Figs. 6a and 7a).

The observation of the inverse-to-normal material behaviour for brittle–ductile transition can be characterised as follows. Specimens deformed at low temperature (25 °C) in a pervasive ductile-like manner with propagating diffuse compaction bands and specimens deforming at a higher temperature (80 °C) by the localised brittle collapse of pores in stationary highly localised compaction bands. Although direct insight into the micro-mechanisms of deformation was not possible at the investigation scale, we attribute this perplexing behaviour to a dominant deformation mode transition. We postulate that a transition from calcite twinning dominated rate-sensitive deformation at low temperatures to a near-rate insensitive Peierls mechanism ideal plastic yield with subsequent brittle failure at high temperature. An alternative explanation to the change in micro-mechanism proposed in the literature (Ghabezloo et al. 2009; Lemos 2003; Renard et al. 2009) cannot be ruled out. Thermal expansion of pore fluid as a trigger for brittle deformation would also explain the observation of temperature-induced weakening by changes in pore pressure facilitating brittle deformation.

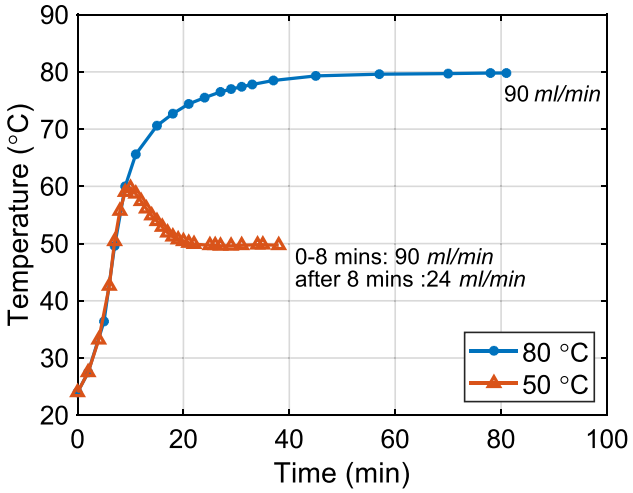


**Fig. 15** The relationship between desired elevated temperature versus time at different flow rates

When fluids rather than gas coexist within the matrix, the problem becomes more complicated. As carbonate rocks are primary sedimentary materials widely distributed in the surface and upper layers of the Earth's surface, the effect of water as pore fluid has been widely studied in the past. Water has been reported to have a significant weakening effect on carbonate rocks' mechanical behaviour, which is the result of several mechanisms (Cai et al. 2019; Ciantia et al. 2015; Liteanu et al. 2013). This water-weakening effect can be accelerated when the temperature is raised (Korsnes et al. 2008; Lisabeth and Zhu 2015; Nicolas et al. 2016). The surface energy reduction by kerosene was also apparent through our experimentation; thus, similar behaviour to that of water in weakening the structure is expected although to a lesser degree. To gain further insight into the micro-mechanism of deformation, future work needs to focus on direct sub-nanoscale time-lapse observations to identify the counterintuitive ductile to brittle transition in Mt Gambier limestone.

## Appendix 1

A series of pre-tests were conducted at a constant water flow rate to warm up the specimen to the desired temperature. The temperature of the specimen was measured with a thermocouple probe made of Cu–CuNi wires which was placed inside the specimen. The thermocouple was connected to ALMEMO 2590 data logger, which has a resolution of 0.1 °C. Figure 15 shows the desired temperature of 80 °C requiring circulating hot water (95 °C) at 90 ml/min

for 60 min and temperature of 50 °C requiring circulating hot water (95 °C) at 90 ml/min for 8 min and then reduced to 24 ml/min for another 30 min until the temperature stabilises. The temperature fluctuation is ±0.5 °C throughout.

## Appendix 2

### Digital Image Processing

Each scan might have slightly different greyscale intensity because of the filament lifetime changes. Differences in greyscale intensity can result in bias when obtaining the accurate registration and thresholding segmentation process across all the images. The greyscale intensity was carefully calibrated according to selected homogeneous regions: air, kerosene, triaxial cell body, top and bottom platens, and rubber sleeve. All differences were corrected using an obtained linear function.

When the X-ray beam passes through a cylindrical specimen, the outer regions absorb and scatter the lower energies in the X-ray spectrum, which results in the exterior regions being brighter than the inner regions. Beam-hardening correlation thus applied a Gaussian smoothing kernel on specified regions of the data to reduce the beam hardening effect (Ketcham and Hanna 2014). Noise is another artifact that makes it challenging to differentiate low-density areas, thereby reducing the ability to segment effectively (Nagarajappa et al. 2015). A nonlinear anisotropic diffusion filter denoising the images and preserving the edges using a similar method by Frangakis and Hegerl (2001) was used in our study.

Image registration is a crucial step in time-lapse experiments. A 3D registration algorithm developed by Latham et al. (2008) was used for image registration. This technique brings two or more images into geometric alignment for further digital image correlation analysis. In our study, each scan was carefully registered to a previous scan to ensure that undeformed parts are overlapped.

The histogram of all the image slices can be exported before image segmentation (Fig. 1). The greyscale values of the tomographs correspond to the X-ray attenuation produced by material, i.e., for example, lower for air than kerosene and the calcite grains. The histogram shows two peaks corresponding to the pores (air, low X-ray attenuation) and matrix (mainly calcite, high X-ray attenuation). With compression of the specimen, the volume of the pore phase reduces, and the matrix phase increases. Two dashed lines indicate the greyscale value of the pore phase and the matrix phase. The converging active contours' (CAC) method was used for the segmentation of these images (Sheppard et al. 2014; Sheppard et al. 2004). This method uses a combination of the watershed and active contour methods to segment the greyscale data. The real boundary of the pore and matrix can be determined by this method. Later on, the layer-by-layer porosity profile can be extracted from the segmented images along with *Z*-axis.

### Digital Image Correlation (DIC) and Digital Volume Correlation (DVC) Analysis

Since the 1980s, the 2D digital image correlation (DIC) technique has been widely used to measure real-time full-field data of displacements and strains (Chu et al. 1985; Vendroux and Knauss 1998). This non-destructive testing method can measure the deformation behaviour of a material over a wide area in exceptional detail. DIC uses image registration algorithms to track the relative displacement of material points between a reference image and a deformed image. Our study uses an open-source 2D subset-based DIC software package: Ncorr (Blaber et al. 2015). Ncorr uses the reliability guided (RG-DIC) method to obtain displacement values for a subset. The shear and compressive strain field can be extracted based on the displacement field using the Green–Lagrangian strain tensor, which can be used to determine the nucleation and propagation of the compaction bands. This DIC code has been shown to work well for tracking the materials displacements (Caselle et al. 2019; Lv et al. 2019; Siddiqui et al. 2021; Stanier et al. 2016). With the wide use of X-ray CT and synchrotron 3D images, the digital volume correlation (DVC) technique has become popular (Bay et al. 1999). This technique can be considered as the extended version of the 2D-DIC method to the 3D-DVC domain in conjunction with 3D images, which effectively determines the internal volumetric deformation behaviours of solid materials. Avizo (Thermofisher Scientific) digital volume correlation (DVC) was used for 3D-DVC analysis in our study. A subset-based (local) approach is used to capture the large displacements on a coarse, regular grid.

## Appendix 3

The radial deformations for both helium and kerosene saturated specimens at low and high temperatures were extracted from every X-ray CT scan. The radial and axial strain versus axial stress is plotted in Fig. 16.

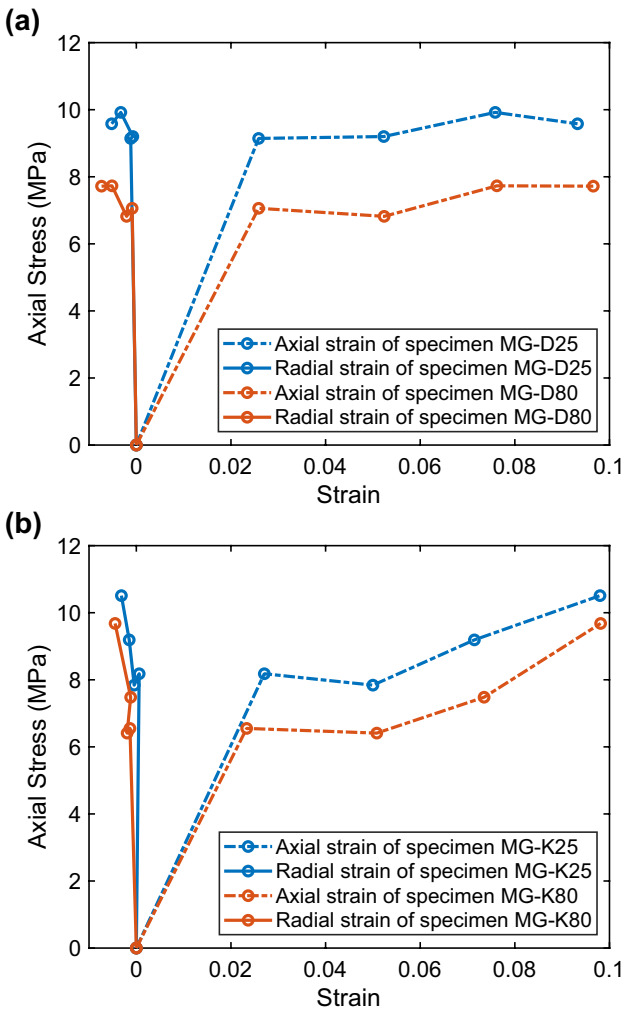


**Fig. 16** The axial and radial strain versus axial stress of **a** specimen MG-D25 (dry 25 °C) and MG-D80 (dry 80 °C) and **b** specimen MG-K25 (kerosene 25 °C) and MG-K80 (kerosene 80 °C)

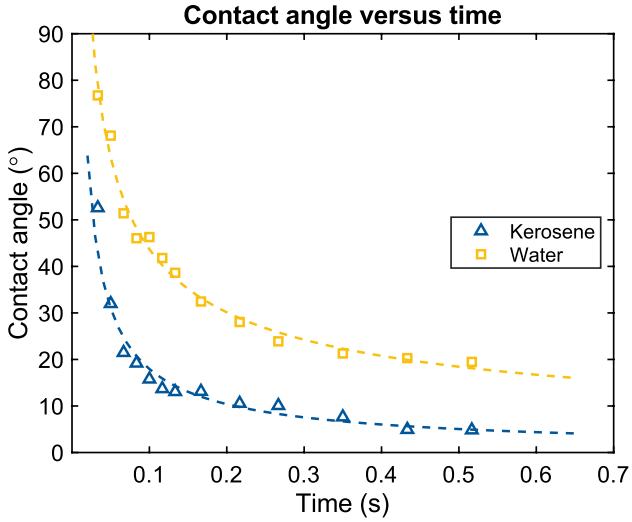


**Fig. 17** Contact angle measurement using distilled water and purified kerosene with crushed powder of Mt Gambier limestone. Because of the highly permeable sample powder, the contact angle of two different fluids was measured using a high-speed camera. The results were plotted by contact angle versus time. Two dashed lines show the power-law fit of the kerosene and water contact angles, respectively

## Appendix 4

The contact angles of kerosene–calcite–air and water–calcite–air were measured by viewing the drop profile (Link and Schlünder 1996; Siddiqui et al. 2019) and are shown in Fig. 17.

The equilibrium contact angle ($\theta_C$) is determined from Young equation (Butt et al. 2013)

$$\gamma_{SG} + \gamma_{SL} + \gamma_{LG}\cos(\theta_C) = 0,$$

where, $\gamma$ is the surface energy, and SG, SL, and LG represent the solid–gas, solid–liquid, and liquid–gas, respectively. We write the contact angle equations for water–calcite–air and kerosene–calcite–air system as

$$\gamma_{Sa} + \gamma_{Sw} + \gamma_{wa}\cos(\theta_w) = 0,$$

$$\gamma_{Sa} + \gamma_{Sk} + \gamma_{ka}\cos(\theta_k) = 0,$$

where Sa, Sw, wa, and w represent calcite–air, calcite–water, water–air, and water, and Sk, ka, and k represent calcite–kerosene, kerosene–air, and kerosene, respectively. The difference between $\gamma_{Sw}$ and $\gamma_{Sk}$ is

$$\Delta\gamma = (\gamma_{Sk} - \gamma_{Sw}) = \gamma_{ka}\cos(\theta_k) - \gamma_{wa}\cos(\theta_w),$$

where $\gamma_{wa}$ is 0.0728 N/m at 25 °C (Lange and Dean 1967) and $\gamma_{ka}$ is 0.0267 N/m at 25 °C (Landry et al. 2011). Also, $\theta_k$ and $\theta_w$ are 5° and 20°, respectively, leading to

$$\Delta\gamma 0.042\mathrm{N/m}.$$

**Acknowledgements** We would like to thank the Tyree X-Ray Laboratory at the School of Mineral and Energy Resources, UNSW for their assistance in imaging and image reconstruction. The project was financially supported by the Australian Research Council (ARC DP170104550, DP170104557, DP200102517, and LP170100233). The first author would like to acknowledge the fellowship from the UNSW Tuition Fee Scholarship (TFS) and the China Scholarship Council (CSC).

**Author Contributions** HR and KRL are project coordinators, proposed the topic, conceived the study, and reviewed the final manuscript. XC conducted the experiments, analysed the data, and composed the draft of the manuscript. All authors read and approved the final manuscript.

**Funding** The project was financially supported by the Australian Research Council (ARC DP170104550, DP170104557, DP200102517, LE200100209, and LP170100233).

**Availability of Data and Materials** The datasets used and/or analysed during the current study are available from the corresponding author on reasonable request.

**Code Availability** Not applicable.

## Declarations

**Conflict of Interest** The authors declare that they have no competing interests.

**Ethics Approval** Not applicable.

**Consent to Participate** Not applicable.

**Consent for Publication** Not applicable.

## References


Abdallah Y, Sulem J, Bornert M, Ghabezloo S, Stefanou I (2021) Compaction banding in high-porosity carbonate rocks: 1. experimental observations. J Geophys Res Solid Earth 126:e2020JB020538. https://doi.org/10.1029/2020JB020538

Anderson GD (1981) Effects of friction on hydraulic fracture growth near unbonded interfaces in rocks. Soc Petrol Eng J 21:21–29. https://doi.org/10.2118/8347-PA

Arzilli F, Cilona A, Mancini L, Tondi E (2016) Using synchrotron X-ray microtomography to characterize the pore network of reservoir rocks: a case study on carbonates. Adv Water Resour 95:254–263. https://doi.org/10.1016/j.advwatres.2015.07.016

Atkinson BK (1984) Subcritical crack growth in geological materials. J Geophys Res Solid Earth 89:4077–4114. https://doi.org/10.1029/JB089iB06p04077

Aydin A, Borja RI, Eichhubl P (2006) Geological and mathematical framework for failure modes in granular rock. J Struct Geol 28:83–98

Baud P, Klein E, Wong T-F (2004) Compaction localization in porous sandstones: spatial evolution of damage and acoustic emission activity. J Struct Geol 26:603–624. https://doi.org/10.1016/j.jsg.2003.09.002

Baud P, Reuschlé T, Ji Y, Cheung CSN, Wong T-F (2015) Mechanical compaction and strain localization in Bleurswiller sandstone. J Geophys Res Solid Earth 120:6501–6522. https://doi.org/10.1002/2015JB012192

Baud P, Vinciguerra S, David C, Cavallo A, Walker E, Reuschlé T (2009) Compaction and failure in high porosity carbonates: mechanical data and microstructural observations. Pure Appl Geophys 166:869–898. https://doi.org/10.1007/s00024-009-0493-2

Baud P, Zhu W, Wong T-F (2000) Failure mode and weakening effect of water on sandstone. J Geophys Res Solid Earth 105:16371–16389. https://doi.org/10.1029/2000jb900087

Baxevanis T, Papamichos E, Flornes O, Larsen I (2006) Compaction bands and induced permeability reduction in Tuffeau de Maastricht calcarenite. Acta Geotech 1:123–135. https://doi.org/10.1007/s11440-006-0011-y

Bay BK, Smith TS, Fyhrie DP, Saad M (1999) Digital volume correlation: three-dimensional strain mapping using X-ray tomography. Exp Mech 39:217–226. https://doi.org/10.1007/BF02323555

Bésuelle P, Rudnicki JW (2004) Localization: shear bands and compaction bands. Int Geophys Ser 89:219–322

Bieniawski ZT (1967) Mechanism of brittle fracture of rock: Part II—experimental studies. Int J Rock Mech Min Sci Geomech Abstr 4:407–423. https://doi.org/10.1016/0148-9062(67)90031-9

Blaber J, Adair B, Antoniou A (2015) Ncorr: open-source 2D digital image correlation matlab software. Exp Mech 55:1105–1122. https://doi.org/10.1007/s11340-015-0009-1

Bourman RP, Murray-Wallace CV, Harvey N (2016) Coastal Landscapes of South Australia. University of Adelaide Press, Adelaide. https://doi.org/10.20851/coast-sa

Brantut N, Heap MJ, Meredith PG, Baud P (2013) Time-dependent cracking and brittle creep in crustal rocks: a review. J Struct Geol 52:17–43. https://doi.org/10.1016/j.jsg.2013.03.007

Brunauer S, Kantro D, Weise C (1956) The surface energies of amorphous silica and hydrous amorphous silica. Can J Chem 34:1483–1496

Burkhard M (1993) Calcite twins, their geometry, appearance and significance as stress–strain markers and indicators of tectonic regime: a review. J Struct Geol 15:351–368. https://doi.org/10.1016/0191-8141(93)90132-T

Butt H-J, Graf K, Kappl M (2013) Physics and chemistry of interfaces. Wiley

Cai X, Zhou Z, Liu K, Du X, Zang H (2019) Water-weakening effects on the mechanical behavior of different rock types: phenomena and mechanisms. Appl Sci 9:4450

Caselle C, Umili G, Bonetto S, Ferrero AM (2019) Application of DIC analysis method to the study of failure initiation in gypsum rocks. Géotech Lett 9:35–45. https://doi.org/10.1680/jgele.18.00156

Cerasi P, Walle LE (2016) Investigation of potential loss of injectivity and formation integrity due to pressure cycling. Energy Procedia 86:420–431. https://doi.org/10.1016/j.egypro.2016.01.043

Charalampidou E-M, Hall SA, Stanchits S, Lewis H, Viggiani G (2011) Characterization of shear and compaction bands in a porous sandstone deformed under triaxial compression. Tectonophysics 503:8–17. https://doi.org/10.1016/j.tecto.2010.09.032

Chen X, Regenauer-Lieb K, Lv A, Hu M, Roshan H (2020a) The dynamic evolution of permeability in compacting carbonates: phase transition and critical points. Transp Porous Media 135:687–711. https://doi.org/10.1007/s11242-020-01493-y

Chen X, Roshan H, Lv A, Hu M, Regenauer-Lieb K (2020b) The dynamic evolution of compaction bands in highly porous carbonates: the role of local heterogeneity for nucleation and propagation. Prog Earth Planet Sci 7:28. https://doi.org/10.1186/s40645-020-00344-0

Chu T, Ranson W, Sutton MA (1985) Applications of digital-image-correlation techniques to experimental mechanics. Exp Mech 25:232–244

Ciantia MO, Castellanza R, Di Prisco C (2015) Experimental study on the water-induced weakening of calcarenites. Rock Mech Rock Eng 48:441–461

Cilona A et al (2014) The effects of rock heterogeneity on compaction localization in porous carbonates. J Struct Geol 67:75–93. https://doi.org/10.1016/j.jsg.2014.07.008

Croize D, Renard F, Gratier J-P (2013) Compaction and porosity reduction in carbonates: a review of observations, theory, and experiments. In: Dmowska R (ed) Advances in geophysics, vol 54. Elsevier, San Diego, pp 181–238. https://doi.org/10.1016/B978-0-12-380940-7.00003-2

Das A, Nguyen GD, Einav I (2011) Compaction bands due to grain crushing in porous rocks: a theoretical approach based on breakage mechanics. J Geophys Res Solid Earth 116:B08203. https://doi.org/10.1029/2011JB008265

Das A, Nguyen GD, Einav I (2013) The propagation of compaction bands in porous rocks based on breakage mechanics. J Geophys Res Solid Earth 118:2049–2066. https://doi.org/10.1002/jgrb.50193

Eberhardt E, Stead D, Stimpson B (1999) Quantifying progressive pre-peak brittle fracture damage in rock during uniaxial compression. Int J Rock Mech Min Sci 36:361–380. https://doi.org/10.1016/S0148-9062(99)00019-4

Ferrill DA, Morris AP, Evans MA, Burkhard M, Groshong RH, Onasch CM (2004) Calcite twin morphology: a low-temperature deformation geothermometer. J Struct Geol 26:1521–1529. https://doi.org/10.1016/j.jsg.2003.11.028

Fortin J, Schubnel A, Guéguen Y (2005) Elastic wave velocities and permeability evolution during compaction of Bleurswiller sandstone. Int J Rock Mech Min Sci 42:873–889. https://doi.org/10.1016/j.ijrmms.2005.05.002

Fossen H, Schultz RA, Shipton ZK, Mair K (2007) Deformation bands in sandstone: a review. J Geol Soc 164:755–769. https://doi.org/10.1144/0016-76492006-036

Fossen H, Soliva R, Ballas G, Trzaskos B, Cavalcante C, Schultz RA (2018) A review of deformation bands in reservoir sandstones: geometries, mechanisms and distribution. Geol Soc Lond Spec Publ 459:9–33

Frangakis AS, Hegerl R (2001) Noise reduction in electron tomographic reconstructions using nonlinear anisotropic diffusion. J Struct Biol 135:239–250. https://doi.org/10.1006/jsbi.2001.4406

Friedman M, Heard HC (1974) Principal stress ratios in cretaceous limestones from Texas Gulf Coast 1. AAPG Bull 58:71–78. https://doi.org/10.1306/83D9137B-16C7-11D7-8645000102C1865D

Ghabezloo S, Sulem JJRM (2009) Stress dependent thermal pressurization of a fluid-saturated rock. Rock Mech Rock Eng 42:1

Griffith AA (1921) VI. The phenomena of rupture and flow in solids. Philos Trans R Soc Lond Ser A 221:163–198

Guéguen Y, Boutéca M (2004) Mechanics of fluid-saturated rocks. Elsevier, Amsterdam

Hadgu T, Zimmerman RW, Bodvarsson GS (1995) Coupled reservoir-wellbore simulation of geothermal reservoir behavior. Geothermics 24:145–166. https://doi.org/10.1016/0375-6505(95)91145-A

Han B, Shen WQ, Xie SY, Shao JF (2019) Influence of pore pressure on plastic deformation and strength of limestone under compressive stress. Acta Geotech 14:535–545. https://doi.org/10.1007/s11440-018-0658-1

Han G, Liu X, Wang E (2013) Experimental study on formation mechanism of compaction bands in weathered rocks with high porosity. Sci China Technol Sci 56:2563–2571. https://doi.org/10.1007/s11431-013-5322-2

Heap M, Baud P, Meredith P (2009) Influence of temperature on brittle creep in sandstones. Geophys Res Lett. https://doi.org/10.1029/2009GL039373

Hellmann R, Renders P, Gratier J, Guiguet R (2002) Experimental pressure solution of chalk in aqueous solutions. Part 2. Deformation examined by SEM, porosimetry, synthetic permeability, and X-ray computerized tomography. In: Roland HeUmann SAW (ed) Water–rock interactions, ore deposits, environmental geochemistry: a tribute to David A. Crerar, vol 7. Geochimical society, St. Louis, pp 153–176

Hill RE (1993) Analysis of deformation bands in the Aztec sandstone, Valley of Fire State Park, Nevada. MS thesis, University of Nevada

Hu M, Schrank C, Regenauer-Lieb K (2020) Cross-diffusion waves in hydro-poro-mechanics. J Mech Phys Solids 135:103632. https://doi.org/10.1016/j.jmps.2019.05.015

Issen K, Rudnicki J (2000) Conditions for compaction bands in porous rock. J Geophys Res Solid Earth 105:21529–21536. https://doi.org/10.1029/2000JB900185

Issen K, Rudnicki J (2001) Theory of compaction bands in porous rock. Phys Chem Earth A 26:95–100. https://doi.org/10.1016/S1464-1895(01)00031-X

Jasinski L, Sangaré D, Adler PM, Mourzenko VV, Thovert JF, Gland N, Békri S (2015) Transport properties of a Bentheim sandstone under deformation. Phys Rev E 91:013304. https://doi.org/10.1103/PhysRevE.91.013304

Karkush M, Zaboon A, Hussien H (2013) Studying the effects of contamination on the geotechnical properties of clayey soil. In: Manassero M, Dominijanni A, Foti S, Musso G (eds) Coupled phenomena in environmental geotechnics. Taylor & Francis, London, pp 599–607

Karner SL, Chester JS, Chester FM, Kronenberg AK, Hajash A Jr (2005) Laboratory deformation of granular quartz sand: implications for the burial of clastic rocks. AAPG Bull 89:603–625. https://doi.org/10.1306/12200404010

Ketcham RA, Hanna RDJC (2014) Beam hardening correction for X-ray computed tomography of heterogeneous natural materials. Comput Geosci 67:49–61

Kingston AM, Myers GR, Latham SJ, Li H, Veldkamp JP, Sheppard AP (2016) Optimized X-ray source scanning trajectories for iterative reconstruction in high cone-angle tomography. In: Stock SR, Müller B, Wang G (eds) Developments in X-ray tomography X. International Society for Optics and Photonics, Bellingham, p 996712. https://doi.org/10.1117/12.2238297

Kodama J, Goto T, Fujii Y, Hagan P (2013) The effects of water content, temperature and loading rate on strength and failure process of frozen rocks. Int J Rock Mech Min Sci 62:1–13. https://doi.org/10.1016/j.ijrmms.2013.03.006

Korsnes RI, Madland MV, Austad T, Haver S, Røsland G (2008) The effects of temperature on the water weakening of chalk by seawater. J Petrol Sci Eng 60:183–193. https://doi.org/10.1016/j.petrol.2007.06.001

Kuempel H-J, Chadha R, Ramana D, Ravi MJJotGSoI, (2017) In-situ pore pressure variations in Koyna–Warna—a promising key to understand triggered earthquakes. J Geol Soc India 90:678–683. https://doi.org/10.1007/s12594-017-0775-8

Kümpel H-J (2012) Thermo-hydro-mechanical coupling in fractured rock. Birkhäuser, Basel. https://doi.org/10.1007/978-3-0348-8083-1

Kümpel HJ (1991) Poroelasticity: parameters reviewed. Geophys J Int 105:783–799. https://doi.org/10.1111/j.1365-246X.1991.tb00813.x

Lackner KS (2002) Carbonate chemistry for sequestering fossil carbon. Ann Rev Energy Environ 27:193–232

Landry CJ, Karpyn ZT, Piri M (2011) Pore-scale analysis of trapped immiscible fluid structures and fluid interfacial areas in oil-wet and water-wet bead packs. Geofluids 11:209–227. https://doi.org/10.1111/j.1468-8123.2011.00333.x

Lange NA, Dean JA (1967) Lange's handbook of chemistry. McGraw-Hill, New York

Latham S, Varslot T, Sheppard A (2008) Image registration: enhancing and calibrating X-ray micro-CT imaging. In: Proceedings of the international symposium of the Society of Core Analysts 2008, Abu Dhabi, UAE. Society of Core Analysts, pp 1–12.

Lemos LJL (2003) Discussion: dynamic thermo-poro-mechanical analysis of catastrophic landslides. Géotechnique 53:523–524. https://doi.org/10.1680/geot.2003.53.5.523

Lenoir N, Andrade J, Sun W, Rudnicki J (2010) In situ permeability measurements inside compaction bands using X-ray CT and lattice Boltzmann calculations. In: Reed KAAAH (ed) Advances in computed tomography for geomaterials: GeoX2020. Wiley, Hoboken, pp 279–286. https://doi.org/10.1002/9781118557723.ch33

Leuthold J, Gerolymatou E, Vergara MR, Triantafyllidis T (2021) Effect of compaction banding on the hydraulic properties of porous rock: part I—experimental investigation. Rock Mech Rock Eng 54:2671–2683. https://doi.org/10.1007/s00603-021-02427-w

Levy M, Bass H, Stern R (2000) Handbook of elastic properties of solids, liquids, and gases, four-volume set. Academic Press, Cambridge

Link KC, Schlünder E-U (1996) A new method for the characterisation of the wettability of powders. Chem Eng Technol 19:432–437. https://doi.org/10.1002/ceat.270190508

Lisabeth HP, Zhu W (2015) Effect of temperature and pore fluid on the strength of porous limestone. J Geophys Res Solid Earth 120:6191–6208. https://doi.org/10.1002/2015JB012152

Liteanu E, Spiers C, De Bresser J (2013) The influence of water and supercritical $CO_2$ on the failure behavior of chalk. Tectonophysics 599:157–169

Lock PA, Jing X, Zimmerman RW, Schlueter EM (2002) Predicting the permeability of sandstone from image analysis of pore structure. J Appl Phys 92:6311–6319. https://doi.org/10.1063/1.1516271

Louis L, Baud P, Wong T-F (2009) Microstructural inhomogeneity and mechanical anisotropy associated with bedding in rothbach sandstone. Pure Appl Geophys 166:1063–1087. https://doi.org/10.1007/s00024-009-0486-1

Louis L, Wong T-F, Baud P, Tembe S (2006) Imaging strain localization by X-ray computed tomography: discrete compaction bands in Diemelstadt sandstone. J Struct Geol 28:762–775. https://doi.org/10.1016/j.jsg.2006.02.006

Lv A, Ramandi HL, Masoumi H, Saadatfar M, Regenauer-Lieb K, Roshan H (2019) Analytical and experimental investigation of pore pressure induced strain softening around boreholes. Int J Rock Mech Min Sci 113:1–10. https://doi.org/10.1016/j.ijrmms.2018.11.001

Mahmutoglu Y (1998) Mechanical behaviour of cyclically heated fine grained rock. Rock Mech Rock Eng 31:169–179

Mavko G, Mukerji T, Dvorkin J (2020) The rock physics handbook. Cambridge University Press, Cambridge

McBeck J, Aiken JM, Ben-Zion Y, Renard F (2020) Predicting the proximity to macroscopic failure using local strain populations from dynamic in situ X-ray tomography triaxial compression experiments on rocks. Earth Planet Sci Lett 543:116344. https://doi.org/10.1016/j.epsl.2020.116344

Mollema P, Antonellini M (1996) Compaction bands: a structural analog for anti-mode I cracks in aeolian sandstone. Tectonophysics 267:209–228. https://doi.org/10.1016/S0040-1951(96)00098-4

Nagarajappa AK, Dwivedi N, Tiwari R (2015) Artifacts: the downturn of CBCT image. J Int Soc Prev Community Dent 5:440–445. https://doi.org/10.4103/2231-0762.170523

Newman GH (1983) The effect of water chemistry on the laboratory compression and permeability characteristics of some north sea chalks. J Petrol Technol 35:976–980. https://doi.org/10.2118/10203-PA

Nicolas A, Fortin J, Regnet J, Dimanov A, Guéguen Y (2016) Brittle and semi-brittle behaviours of a carbonate rock: influence of water and temperature. Geophys J Int 206:438–456. https://doi.org/10.1093/gji/ggw154

Oka F, Kitahara H, Ohta H (2006) Observation of compaction bands under triaxial conditions for diatomaceous mudstone. In: Geomechanics and geotechnics of particulate media: proceedings of the international symposium on geomechanics and geotechnics of particulate media, Ube, Japan, 12–14 September 2006. CRC Press, p 69.

Olsson WA (1999) Theoretical and experimental investigation of compaction bands in porous rock. J Geophys Res Solid Earth 104:7219–7228. https://doi.org/10.1029/1998JB900120

Paluszny A et al (2020) Caprock integrity and public perception studies of carbon storage in depleted hydrocarbon reservoirs. Int J Greenh Gas Control 98:103057. https://doi.org/10.1016/j.ijggc.2020.103057

Parlangeau C, Dimanov A, Lacombe O, Hallais S, Daniel JM (2019) Uniaxial compression of calcite single crystals at room temperature: insights into twinning activation and development. Solid Earth 10:307–316. https://doi.org/10.5194/se-10-307-2019

Plummer LN, Busenberg E (1982) The solubilities of calcite, aragonite and vaterite in $CO_2$–$H_2O$ solutions between 0 and 90°C, and an evaluation of the aqueous model for the system $CaCO_3$–$CO_2$–$H_2O$. Geochim Cosmochim Acta 46:1011–1040. https://doi.org/10.1016/0016-7037(82)90056-4

Pons A, David C, Fortin J, Stanchits S, Menéndez B, Mengus J (2011) X-ray imaging of water motion during capillary imbibition: a study on how compaction bands impact fluid flow in Bentheim sandstone. J Geophys Res Solid Earth. https://doi.org/10.1029/2010JB007972

Rashid F, Glover PWJ, Lorinczi P, Hussein D, Lawrence JA (2017) Microstructural controls on reservoir quality in tight oil carbonate reservoir rocks. J Petrol Sci Eng 156:814–826. https://doi.org/10.1016/j.petrol.2017.06.056

Regenauer-Lieb K et al (2020) Cross-diffusion waves as a trigger for multiscale, multiphysics Instabilities: application to earthquakes. Solid Earth Discuss 2020:1–44. https://doi.org/10.5194/se-2020-149

Renard F, Bernard D, Desrues J, Ougier-Simonin A (2009) 3D imaging of fracture propagation using synchrotron X-ray microtomography. Earth Planet Sci Lett 286:285–291. https://doi.org/10.1016/j.epsl.2009.06.040

Renner J, Rummel F (1996) The effect of experimental and microstructural parameters on the transition from brittle failure to cataclastic flow of carbonate rocks. Tectonophysics 258:151–169. https://doi.org/10.1016/0040-1951(95)00192-1

Rice JR (2006) Heating and weakening of faults during earthquake slip. J Geophys Res Solid Earth. https://doi.org/10.1029/2005JB004006

Risnes R, Haghighi H, Korsnes RI, Natvik O (2003) Chalk–fluid interactions with glycol and brines. Tectonophysics 370:213–226. https://doi.org/10.1016/S0040-1951(03)00187-2

Risnes R, Madland MV, Hole M, Kwabiah NK (2005) Water weakening of chalk—mechanical effects of water–glycol mixtures. J Petrol Sci Eng 48:21–36. https://doi.org/10.1016/j.petrol.2005.04.004

Robinson L (1959) Effects of pore and confining pressures on failure characteristics of sedimentary rocks. Transactions of the AIME 216:26–32

Roshan H, Aghighi MA (2012) Chemo-poroelastic analysis of pore pressure and stress distribution around a wellbore in swelling shale: effect of undrained response and horizontal permeability anisotropy. Geomech Geoeng 7:209–218. https://doi.org/10.1080/17486025.2011.616936

Roshan H, Chen X, Pirzada MA, Regenauer-Lieb K (2019) Permeability measurements during triaxial and direct shear loading using a novel X-ray transparent apparatus: fractured shale examples from Beetaloo basin, Australia. NDT&E Int 107:102129. https://doi.org/10.1016/j.ndteint.2019.102129

Roshan H, Rahman S (2011) A fully coupled chemo-poroelastic analysis of pore pressure and stress distribution around a wellbore in water active rocks. Rock Mech Rock Eng 44:199–210

Rostom F, Røyne A, Dysthe DK, Renard F (2013) Effect of fluid salinity on subcritical crack propagation in calcite. Tectonophysics 583:68–75. https://doi.org/10.1016/j.tecto.2012.10.023

Rowe K, Rutter E (1990) Palaeostress estimation using calcite twinning: experimental calibration and application to nature. J Struct Geol 12:1–17. https://doi.org/10.1016/0191-8141(90)90044-Y

Røyne A, Bisschop J, Dysthe DK (2011) Experimental investigation of surface energy and subcritical crack growth in calcite. J Geophys Res Solid Earth. https://doi.org/10.1029/2010JB008033

Rustichelli A, Tondi E, Agosta F, Cilona A, Giorgioni M (2012) Development and distribution of bed-parallel compaction bands and pressure solution seams in carbonates (Bolognano Formation, Majella Mountain, Italy). J Struct Geol 37:181–199. https://doi.org/10.1016/j.jsg.2012.01.007

Sayers CM (2008) The elastic properties of carbonates. Lead Edge 27:1020–1024. https://doi.org/10.1190/1.2967555

Sengun N (2014) Influence of thermal damage on the physical and mechanical properties of carbonate rocks. Arab J Geosci 7:5543–5551. https://doi.org/10.1007/s12517-013-1177-x

Shahin G, Viggiani G, Buscarnera G (2020) Simulating spatial heterogeneity through a CT-FE mapping scheme discloses boundary effects on emerging compaction bands. Int J Solids Struct 206:247–261. https://doi.org/10.1016/j.ijsolstr.2020.08.016

Sheppard A et al (2014) Techniques in helical scanning, dynamic imaging and image segmentation for improved quantitative analysis with X-ray micro-CT. Nucl Instrum Methods Phys Res Sect B Beam Interact Mater Atoms 324:49–56. https://doi.org/10.1016/j.nimb.2013.08.072

Sheppard AP, Sok RM, Averdunk H (2004) Techniques for image enhancement and segmentation of tomographic images of porous materials. Phys A Stat Mech Appl 339:145–151. https://doi.org/10.1016/j.physa.2004.03.057

Siddiqui MAQ, Chen X, Iglauer S, Roshan H (2019) A multiscale study on shale wettability: spontaneous imbibition versus contact angle. Water Resour Res 55:5012–5032. https://doi.org/10.1029/2019WR024893

Siddiqui MAQ, Salvemini F, Ramandi HL, Fitzgerald P, Roshan H (2021) Configurational diffusion transport of water and oil in dual continuum shales. Sci Rep 11:2152. https://doi.org/10.1038/s41598-021-81004-1

Skoczylas N (2015) Determining the gas permeability coefficient of a porous medium by means of the bubble-counting flow meter. Meas Sci Technol 26:085004. https://doi.org/10.1088/0957-0233/26/8/085004

Sly MK, Thind AS, Mishra R, Flores KM, Skemer P (2020) Low-temperature rheology of calcite. Geophys J Int 221:129–141. https://doi.org/10.1093/gji/ggz577

Somerton WH (1992) Thermal properties and temperature-related behavior of rock/fluid systems. Elsevier, Amsterdam

Stanier SA, Blaber J, Take WA, White D (2016) Improved image-based deformation measurement for geotechnical applications. Can Geotech J 53:727–739

Sternlof KR, Karimi-Fard M, Pollard DD, Durlofsky LJ (2006) Flow and transport effects of compaction bands in sandstone at scales relevant to aquifer and reservoir management. Water Resour Res. https://doi.org/10.1029/2005WR004664

Sternlof KR, Rudnicki JW, Pollard DD (2005) Anticrack inclusion model for compaction bands in sandstone. J Geophys Res Solid Earth 110:B11403. https://doi.org/10.1029/2005JB003764

Sulem J, Lazar P, Vardoulakis I (2007) Thermo-poro-mechanical properties of clayey gouge and application to rapid fault shearing. Int J Numer Anal Methods Geomech 31:523–540

Sulem J, Stefanou I (2016) Thermal and chemical effects in shear and compaction bands. Geomech Energy Environ 6:4–21

Takano D, Lenoir N, Otani J, Hall SA (2015) Localised deformation in a wide-grained sand under triaxial compression revealed by X-ray tomography and digital image correlation. Soils Found 55:906–915. https://doi.org/10.1016/j.sandf.2015.06.020

Tanikawa W, Shimamoto T (2006) Klinkenberg effect for gas permeability and its comparison to water permeability for porous sedimentary rocks. Hydrol Earth Syst Sci Discuss 3:1315–1338. https://doi.org/10.5194/hessd-3-1315-2006

Tembe S, Baud P, Wong TF (2008) Stress conditions for the propagation of discrete compaction bands in porous sandstone. J Geophys Res Solid Earth 113:B09409. https://doi.org/10.1029/2007JB005439

Tembe S, Vajdova V, Wong TF, Zhu W (2006) Initiation and propagation of strain localization in circumferentially notched samples of two porous sandstones. J Geophys Res Solid Earth 111:B02409. https://doi.org/10.1029/2005JB003611

Tondi E, Antonellini M, Aydin A, Marchegiani L, Cello G (2006) The role of deformation bands, stylolites and sheared stylolites in fault development in carbonate grainstones of Majella Mountain, Italy. J Struct Geol 28:376–391. https://doi.org/10.1016/j.jsg.2005.12.001

Turner FJ, Griggs DT, Heard H (1954) Experimental deformation of calcite crystals. Geol Soc Am Bull 65:883–934

Vajdova V, Wong TF (2003) Incremental propagation of discrete compaction bands: acoustic emission and microstructural observations on circumferentially notched samples of Bentheim. Geophys Res Lett. https://doi.org/10.1029/2003GL017750

Varslot T, Kingston A, Sheppard A, Sakellariou A (2010) Fast high-resolution micro-CT with exact reconstruction methods. In: The SPIE—progress in biomedical optics and imaging, San Diego, California, USA, 2010. International Society for Optics and Photonics, p 780413. https://doi.org/10.1117/12.860298

Vendroux G, Knauss W (1998) Submicron deformation field measurements: part 2 improved digital image correlation. Exp Mech 38:86–92

Viggiani G, Tengattini A (2019) Recent developments in laboratory testing of geomaterials with emphasis on imaging. In: Proceedings of the XVII ECSMGE-2019. The Icelandic Geotechnical Society, Reykjavik

Violay M, Di Toro G, Nielsen S, Spagnuolo E, Burg JP (2015) Thermo-mechanical pressurization of experimental faults in cohesive rocks during seismic slip. Earth Planet Sci Lett 429:1–10. https://doi.org/10.1016/j.epsl.2015.07.054

Violay M et al (2014) Effect of water on the frictional behavior of cohesive rocks during earthquakes. Geology 42:27–30. https://doi.org/10.1130/G34916.1

Walsh JB (1965) The effect of cracks on the compressibility of rock. J Geophys Res Solid Earth 70:381–389. https://doi.org/10.1029/JZ070i002p00381

Wang B, Chen Y, Wong T-F (2008) A discrete element model for the development of compaction localization in granular rock. J Geophys Res Atmos. https://doi.org/10.1029/2006JB004501

Wawersik WR et al (2001) Terrestrial sequestration of $CO_2$: an assessment of research needs. In: Dmowska R, Saltzman B (eds) Advances in Geophysics, vol 43. Elsevier, Amsterdam, pp 97–IX. https://doi.org/10.1016/S0065-2687(01)80003-0

Wiederhorn SM (1967) Influence of water vapor on crack propagation in soda-lime glass. J Am Ceram Soc 50:407–414. https://doi.org/10.1111/j.1151-2916.1967.tb15145.x

Wong LNY, Zhang Y, Wu Z (2020) Rock strengthening or weakening upon heating in the mild temperature range? Eng Geol 272:105619. https://doi.org/10.1016/j.enggeo.2020.105619

Wong TF, David C, Zhu W (1997) The transition from brittle faulting to cataclastic flow in porous sandstones: mechanical deformation. J Geophys Res Solid Earth 102:3009–3025. https://doi.org/10.1029/96JB03281

Xue L, Qin S, Sun Q, Wang Y, Lee LM, Li W (2014) A study on crack damage stress thresholds of different rock types based on uniaxial compression tests. Rock Mech Rock Eng 47:1183–1195. https://doi.org/10.1007/s00603-013-0479-3

Yavuz H, Demirdag S, Caran S (2010) Thermal effect on the physical properties of carbonate rocks. Int J Rock Mech Min Sci 47:94–103. https://doi.org/10.1016/j.ijrmms.2009.09.014

Zeng L, Chen Y, Lu Y, Hossain MM, Saeedi A, Xie Q (2020) Role of brine composition on rock surface energy and its implications for subcritical crack growth in calcite. J Mol Liq 303:112638. https://doi.org/10.1016/j.molliq.2020.112638

Zhou S, Xia C, Zhou Y (2018) A theoretical approach to quantify the effect of random cracks on rock deformation in uniaxial compression. J Geophys Eng 15:627–637. https://doi.org/10.1088/1742-2140/aaa1ad

Zimmerman RW (2000) Coupling in poroelasticity and thermoelasticity. Int J Rock Mech Min Sci 37:79–87. https://doi.org/10.1016/S1365-1609(99)00094-5